PETROPHYSICAL CHARACTERIZATION OF DEEP, LOW-PERMEABILITY

CARBONATE FORMATIONS IN TARIM OILFIELD

A Thesis

by

XINYANG WU

Submitted to the Office of Graduate and Professional Studies of
Texas A&M University
in partial fulfillment of the requirements for the degree of

MASTER OF SCIENCE

Chair of Committee,	I. Yucel Akkutlu
Committee Members,	Walter B. Ayers
	Lisa M. Perez
Head of Department,	A. Daniel Hill

December 2015

Major Subject: Petroleum Engineering

ABSTRACT

The paper presents a petrophysical modeling and permeability analysis approach for a tight carbonate formation. The formation samples used in this study are from the Tarim oil field Yingshan formation, deposited during Ordovician in the Tarim basin of Southern Xinjiang in Northwest China. The petrophysical modeling is based on a detailed pore structure analysis utilizing thin sections, focused ion-beam SEM images, XRD, and nitrogen and helium porosimetry data. A permeability analysis was performed after the pore structure was characterized. Rock samples from three wells are analyzed. Lab experiments indicate that the samples are rich in carbonate (typically more than 90%) and experienced diagenesis characterized by cementation associated with dolomitization and healed natural fractures. No significant pore volume is observed in thin section images. Nonetheless, SEM images and nitrogen porosimetry both show that matrix pore volume consists of micro-, meso- and macro-pores. Porosimetry data indicate that most of the rock samples are rich in meso- and macropores with an effective pore size of 60-90 nanometers; 34-80% of total matrix pore volume is due to these pores, while the rest of the pore volume is due to natural fractures and larger pores that have not been captured by nitrogen porosimetry. The petrophysical analysis suggests that reliable reservoir storage and flow models to predict the well performances in the field need to be triple porosity, including re-opened fractures imbedded within a matrix that includes meso and macropores. This thesis is a preparation for the next phase of "Petrophysical Characterization of Deep Low Permeability Carbonate Formations for Fluid Storage and Transport Predictions in Tarim Oilfield" which will include a brief

description of a single well numerical model with hydraulic fracture to simulate the

base-case production trends from the region and compare with the wells' performances.

ACKNOWLEDGEMENTS

TABLE OF CONTENTS

LIST OF FIGURES

LIST OF TABLES

INTRODUCTION

Located in Northwest China within the Xinjiang province, Tarim basin is considered to have huge potential for future oil and gas production. Numerically speaking, the petroleum unproven reserve estimations of the Tarim basin are 1.75 billion barrels (11 billion cubic meter) of oil and 282 TCF (7.98 trillion cubic meter) of natural gas (Chai 1991), which is about 1% of U.S. oil and 15% of U.S. gas unproved resources as of year 2012 (EIA report 2012). With such huge petroleum resource, especially in natural gas, Tarim basin is becoming a new area of interest for the oil and gas industry. Also, the unique petrophysical properties make this area eye-catching in the petrophysics field.

Figure 1 displays the general setting of Tarim basin. The basin is surrounded by Tian Shan Mountain Range in the north, Kunlun Mountain Range in the southwest and Altun Mountain Range in the southeast. The area of interest in this thesis is bounded by the red rectangle in the middle of Taklamagan Desert in Figure 1. The target area is also known as Ta Zhong #10 band, within which the geological and petrophysical properties are believed to be uniform, according to Tarim Oil Company. In addition to the amount of hydrocarbons in Tarim basin, the unique matrix structure also draws attention from industry. At the time this thesis work initiated, the only information revealed about Tarim reservoir matrices is that at the depth of interest (about 20,000 ft), the pressure should be extremely high such that the reservoir matrix and pore structure might be transformed and deviated from the original matrix and pore structure, and such transformation requires in-depth study on how to integral the new pore network into the reservoir simulation.
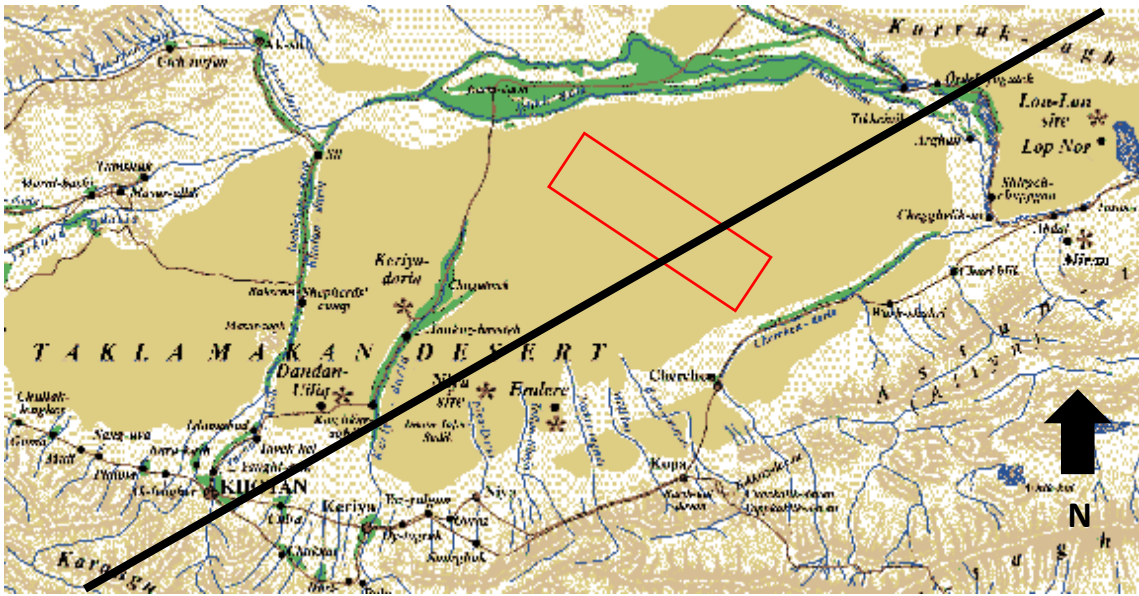
Figure 1. Map of Tarim Basin. Red rectangle indicates the location of Ta Zhong #10 band, which is the area of interest in this study. Adapted from Rust (2001).

Four wells have been studied for petrophysics; the names of these well are concealed due to confidential purpose. Thus these wells are named well A, B, C and D in this thesis. The information from well D was limited and we were provided only with the thin section images so that no further research could be done related to this well. Wells A, B and C are indicated by red arrows in Figure 2. Well D, though not shown up in Figure 2, is very close to well B. Wells A and B are both in TZ #10 band, which is the irregular yellow-colored area elongated NW-SE direction in Figure 2 and the red rectangular area in Figure 1. In this thesis, a petrophysical modeling approach will be presented in detail for well A. The results for the other wells will be included but the analysis procedure is similar to well A.

Figure 2 shows a more detailed geological map of the red rctangular area in Figure 1. The three red arrows indicate the position of three wells studied in this study, from left to right are: well B, well A and well C. Tarim basin is surrounded by three mountain ranges and has relatively low elevation. The area of interest, Ta Zhong # 10 band, is believed to have uniform geological and reservoir properties, such as rock composition, porosity,
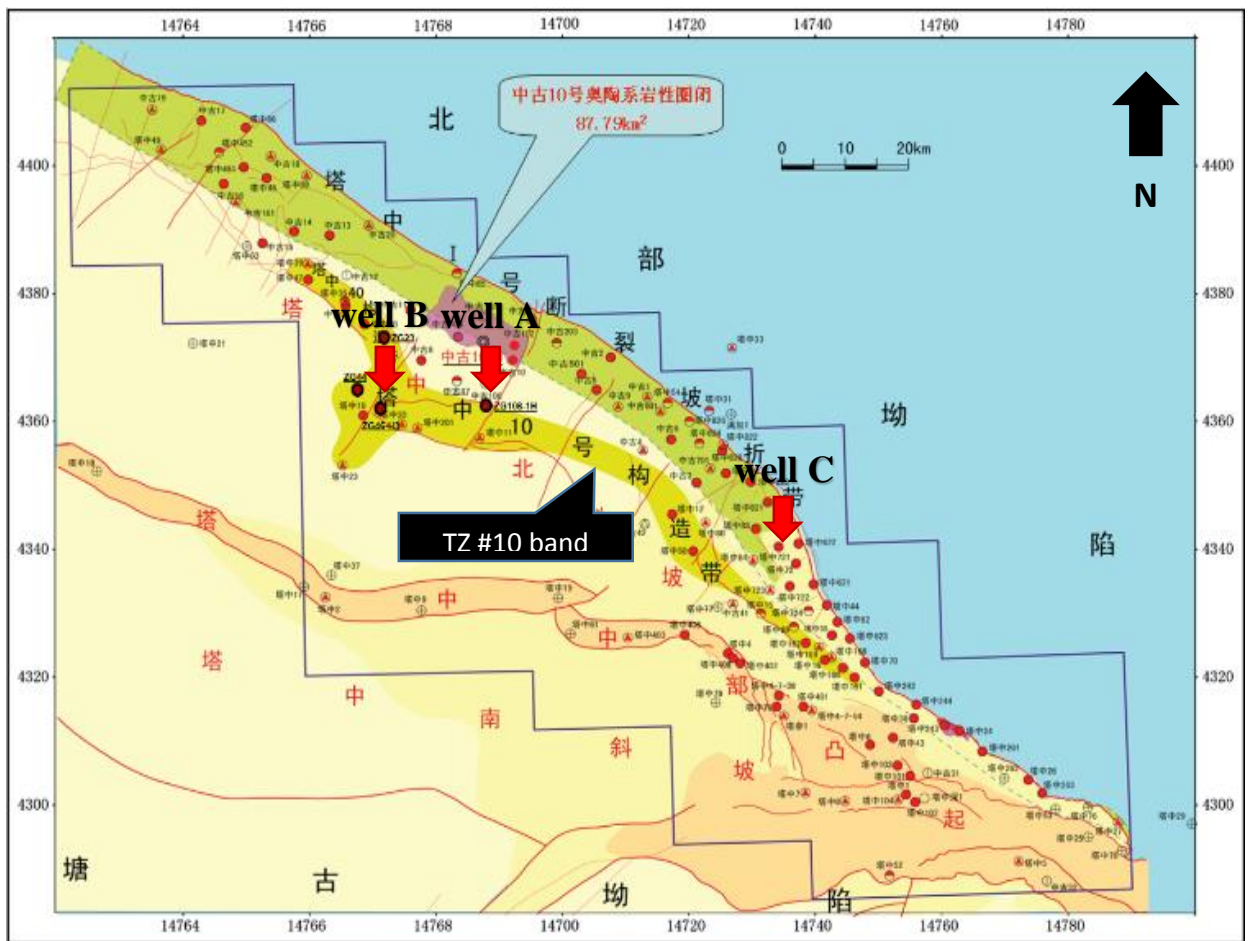
Figure 2. Tarim oilfield geological map showing elevated area in the middle, depression in NE and SW.

permeability and etc. To the north of Ta Zhong #10 band is the Northern depression, indicated as the light blue-colored area, and to the south is the Tang Gu depression, shown in SW corner in Figure 2. In short, Ta Zhong #10 band forms an anticline in a relatively low elevation area.

Problem Identification

Reservoir flow simulation using a commercial software is a mature and widely-used tool for predicting the production from a well or a whole field. An accurate simulation of the Tarim oil field's production wells requires geological and petrophysical models of the formation. The formation of interest to this study is an extremely deep (about 20,000 ft), low-porosity and –permeability carbonate formation. Although this formation has been investigated using various types of data over the years, no petrophysical model currently exists for the simulation task.

This thesis focuses on providing a conceptual petrophysical model for an accurate reservoir simulation analysis. This work aims at understanding the geological background of the field and the area of interest, characterizing the matrix pore structure of the carbonate formation and evaluating the rock for its potential to store and transport fluids. More specifically, the problems need to be solved are: complex geological background information, unique matrix component, pore structure and texture under particularly high pressure due to high depth, unknown pore sizes and pore structure distributions and how to integrate these factors together in one petrophysical model.

Moreover, this study also provides the permeability analysis of this formation using a porosity-permeability relationship, and assuming capillary tube model. Calculated results are compared with the measured permeability results and the difference between these two values will be explained.

GEOLOGICAL BACKGROUND INFORMATION

This section provides a more detailed discussion on geological background. Bosboom (2011) indicated that Tarim Basin experienced a transition from marine to continent depositional environment, on the basis of biostratigraphic and lithostratigraphic studies. Core samples from Tarim Basin included marine fossils, such as ostracods and bivalves. Secondly, strong lithostratigraphic similarity between central Asia and Europe proved that paleoocean covered vast majority of Eurasia continent, including Tarim Basin. The paleo-ocean, or the Tarim Sea, started retreating during the early Eocene and finished retreating during the late Oligocene. Following late Oligocene, the Tarim Sea became Tarim Basin. Figure 3 shows the retreating of the Tarim Sea and forming of the Tarim Basin. The payzone formation of TZ #10 band was deposited during late Cambrian to Ordovician, far before the Tarim Sea started retreating (He et al. 2015).

Sea-level change was the most important controlling factor to the evolution of Cambrian- Ordovician sedimentary facies in the middle to eastern Tarim Basin (He et al. 2015). The deposited environment of TZ #10 band in Tarim Basin is the margin of weak rimmed carbonate platform (He et al. 2015), the cross-sectional picture of carbonate platform is displayed in Figure 4. The platform-margin system usually includes marginal reefs and platform-margin slope. Within the system, reef and inclined slope are high dynamic energy areas where good reservoir quality is expected. Combining the information from Figure 2, He et al.'s paper and well B drilling report, the initial presumption for Tarim Oilfield, especially the three wells being reported, is that the area circled by purple line is the ancient platform margin. Wells A and B are both drilled in

the reef where supposed to be favorable reservoirs. Well C is drilled in the ancient slope area where the energy level was high, small particles on the slope are taken away by waves, or well C is drilled in the deep-water, low energy area. Further investigations are needed to answer this question.

Along the bulk black line in Figure 1 the cross sectional view during deposition is believed to be similar to Figure 3b. Ta Zhong #10 band (wells A and B) are completed in the ancient reef. Well C is located in marginal slope or deep-water environment. Based on the log interpretations by Tarim Oil Company, the payzones of wells A, B and C were all from the same formation, Yingshan formation.

In platform margin reef and/or slope, diagenesis played a significant role in reservoir. Dolomitization of calcite to dolostone may have led to an increase or decrease in porosity (Purser et al. 1994). The dolostone type in Ta Zhong # 10 band is considered to be hydrothermal
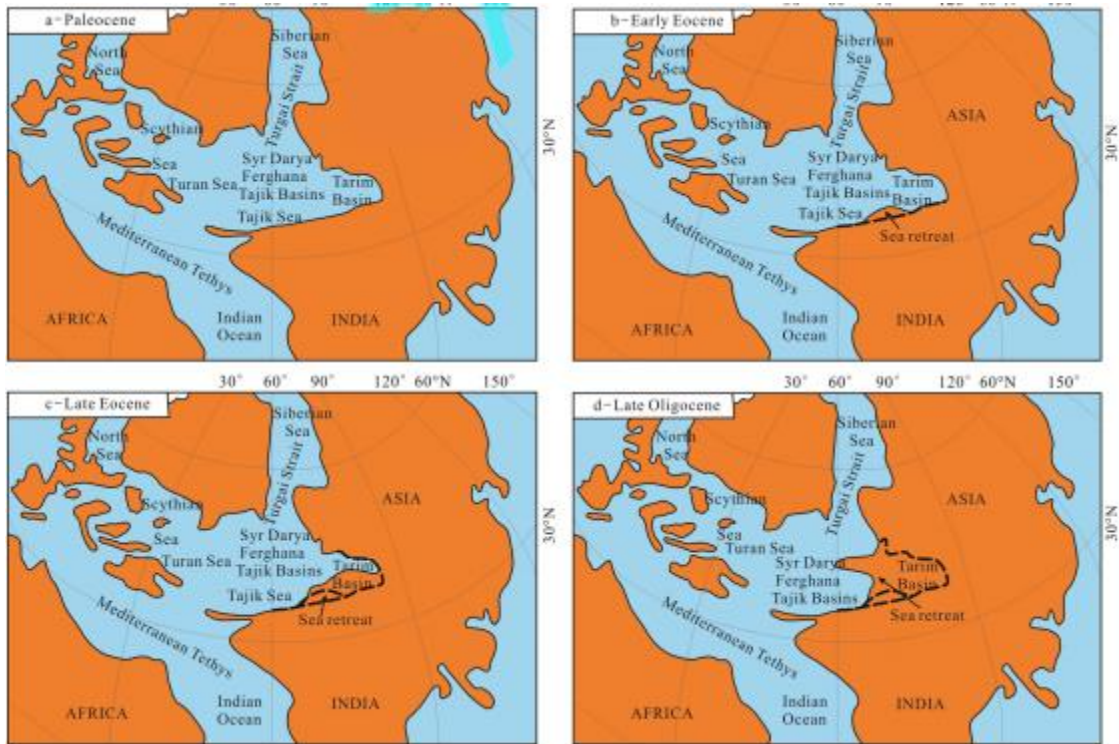
Figure 3. Schematic diagram of the closure of Tarim Sea. Reprinted from Bosboom (2011).

dolostone, which is formed by replacing carbonate with hydrothermal fluids from deep crust. Therefore, dolomite was precipitated along the fluid paths and hydrothermal dolostone was formed. As a result, hydrothermal dolostone is distributed along fractures and unconformities.
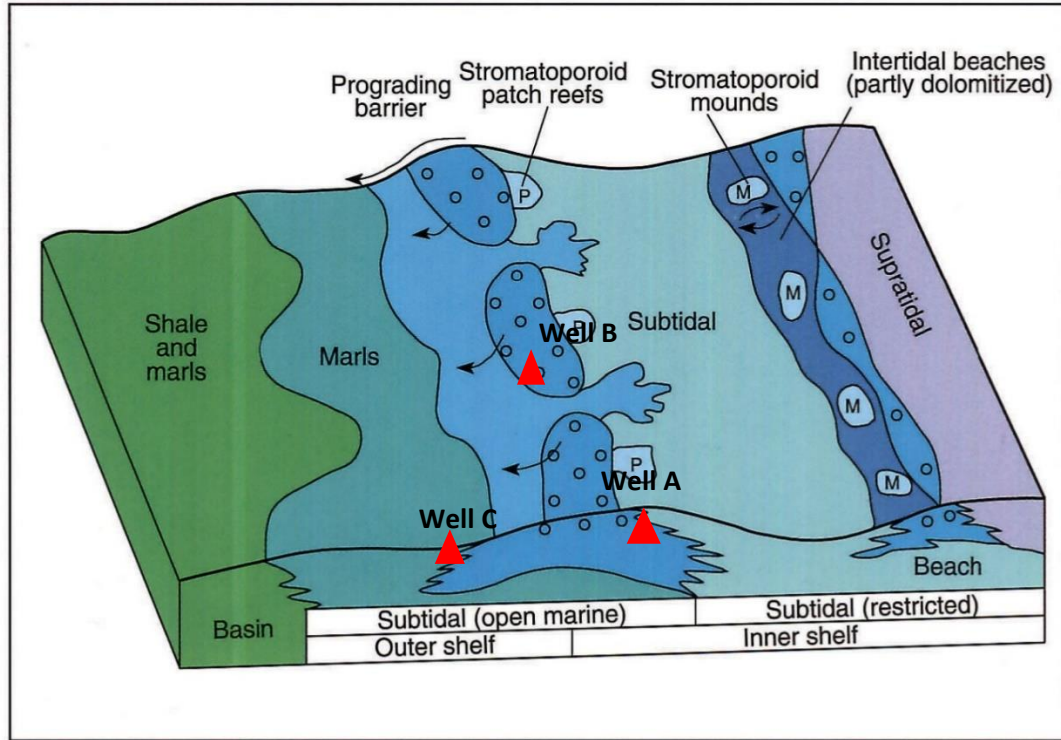
Figure 4. Cross-sectional diagram of Tarim Oilfield Ordovician reservoir depositional system. Adapeted from Halbertsma (2012).

METHODOLOGY

The methodologies used in this study include thin section analysis, ion-beam SEM image interpretation, XRD interpretation, and nitrogen and helium porosimetry. These four methodologies were used to achieve different objectives. Thin sections are used to obtain a direct pictures of formation core samples, by increasing the magnification, more detailed pictures of rock samples at certain depth were collected. Thin section pictures cannot go beyond certain magnification (about 50X) and few pores are observed at the maximum magnification. Therefore, ion-beam SEM images were utilized to capture more detailed information of rock samples (for instance, micropores, kerogen and etc.). SEM images verified the existence of micropores and, therefore, the feasibility of this research. Nitrogen porosimetry was used to quantify the volume of micropores and pore size distribution. Moreover, XRD and helium porosimetry were also used to measure the rock composition and total porosity, which are independent of the other methods. By integrating the results of these methods, a complete petrophysical analysis was performed.

The physics behind the tools, the purpose and the working procedure of each tool will be discussed in detail except for Helium Porosimetry since it has been used to measure porosity for decades and is quite familiar to all petroleum engineers.

Thin Section

In general, thin section image is a picture of polished rock slice taken under polarized microscope. Compared with non-polarized microscope which uses visible (natural) light

as light resource in which light wave vibrates from all directions, polarized microscope allows only one direction of wave vibration going through the rock sample. Within the thin slice of rock, different mineral components have distinct reflection frequencies (Chayes 1954). By exposing the rock sample in one direction of light wave and collecting the reflections, the amount and composition of each component of the rock could be clearly observed without interference.

The procedures of conducting a thin section experiment includes cutting the rock into a thin slice (about 30 μm), polishing the rock surface, gluing the rock sample to glass slide and then put another cover slip on top of the rock sample. When pasting the rock chip onto glass slide using epoxy, it is important that no gas bubble is left between the rock and the layers of epoxy. Some rock samples are porous such that the epoxy on bottom would travel through the pores, reach to the top and stick to the epoxy on top. When placing the cover slip on top of the top epoxy, it may be necessary to move it around to expel gas bubbles. Glass slide, rock chip and cover slip should all be put on hot plate to eliminate the contaminations before using in experiments. After the rock sample is fully prepared, the glass slide could be put under polarized microscope to observe the thin section images (Hirsch 2012).

Figure 6 is a thin section image taken from well A sample. In Figure 6, it is clear that there are at least three types of minerals: the brown-colored rock occupying major part of the image, the white-colored rock filling the space between brown-colored rock and the dark yellow band on the bottom of this image.
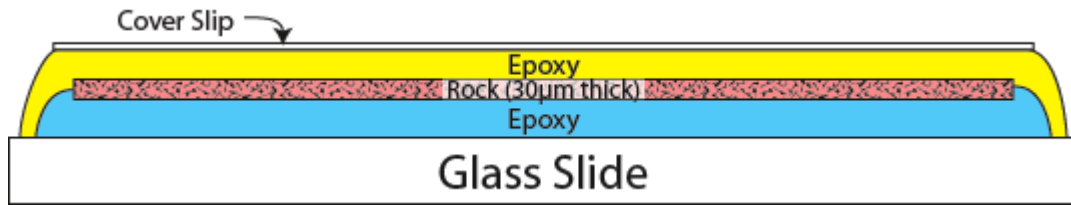
Figure 5. Schematic of thin section from side view. Reprinted from Hirsch (2012).

Also, along the band on the bottom, the two pink lines, which are colored after the picture is taken, indicate fractures. No pores were observed under the current magnification. At current stage, the most responsible and efficient way is using higher magnification two options are available if we would like to see a clearer image: use higher magnification or another instrument. Since these thin section images are provided by Tarim Oil Company and images under higher magnification are not available, we decided to use ion-beam SEM image.
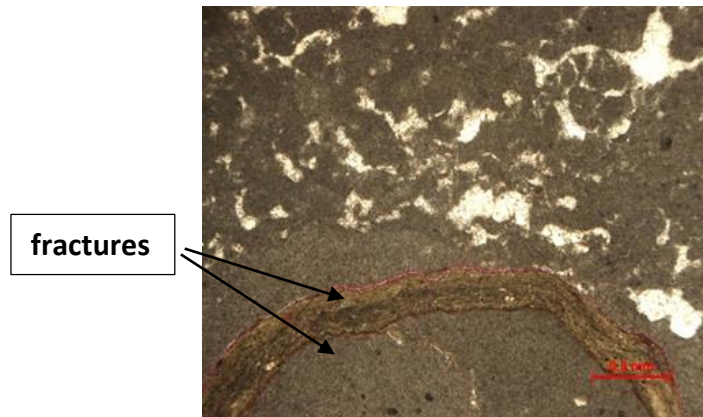
Figure 6. Thin section image example

SEM Image

A Scanning Electron Microscope (SEM) shoots a beam of high-energy electrons to create a range of signals at the rock sample surface. The signals that derive from electron-sample interactions disclose information about the rock sample, including surface morphology (texture), chemical composition, crystal structure and orientation of materials making up the sample. In this study, data were collected over a selected area (smaller than 4 mm^2) of the rock sample surface, and a 2-D image was generated that presents spatial variations in these rock samples. The procedure of using SEM is very similar to that of thin section, the main difference is that SEM requires a much smoother surface. A certain polishing apparatus is used such that SEM could provide a clear image of desired surface. Also, the thickness of rock sample in SEM is much larger than that of thin section. As long as the rock sample could be put inside the holder of the polishing apparatus (about 2mm), SEM will provide good images of rock sample surface.

The colors in SEM images are inversely proportional to surface densities. More specifically, pores are pure black, organic matters such as bitumen and kerogen (if there is any) are dark gray and clay minerals are light gray in SEM images in general. The magnification of SEM ranges from 20X to approximately 30,000X, with a spatial resolution of 50 to 100 nm (Swapp 2012). The SEM instrument is also capable of performing other analyses, such as chemical composition, which will not be discussed in this paper. Figure 7 shows two SEM images of Tarim rock samples. It clearly demonstrates that, as the magnification increases, a larger number of pores are visible in
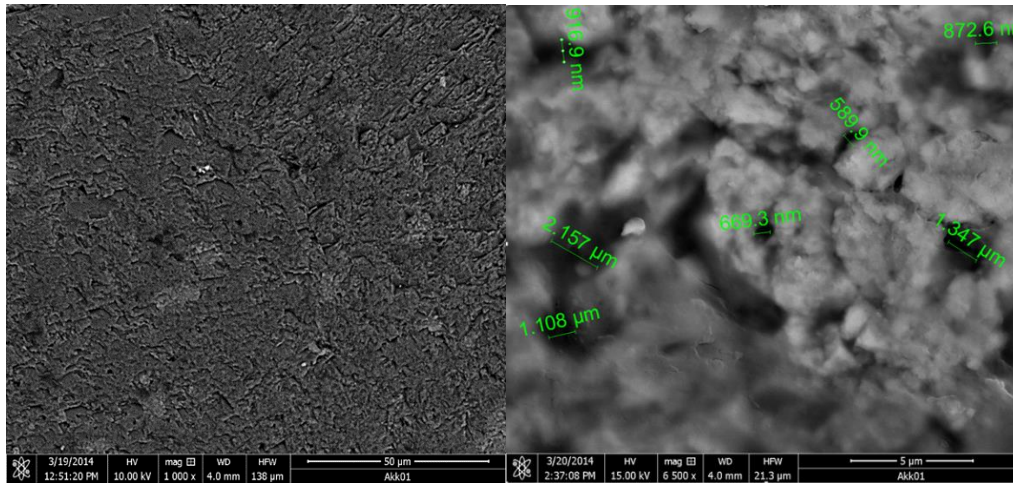
Figure 7. SEM images (low and high magnifications)

the images. In essence, these images verify the existence of small pores and indicate that the absence of pores in thin section images was due to the low magnification.

XRD Interpretation

X-ray powder diffraction (XRD) is a fast analytical method used for material phase identification and can provide information on unit cell dimensions. XRD is based on constructive interference of monochromatic x-rays and a crystalline sample. The x-rays are generated to produce monochromatic radiation directly toward the sample. The interactions between the x-rays and the rock samples produce constructive interference when satisfying Bragg's Law, which is $n\lambda = 2d \sin \theta$. These diffracted x-rays are then perceived, processed and calculated. By comparing the sample angles within a range of 2θ angles and finding analog, the materials being tested and their composition could be determined. Because XRD works based on the interaction between x-ray and crystals

inside the sample, rock sample needs to be grounded before sending to XRD

instruments. Moreover, XRD could not be used to test organic matters and is of

relatively low accuracy in sandstone.

XRD result provides the composition and the density of the rock sample. As displayed in

Figure 8, by matching the peaks from the rock sample and the peaks from a database, it

is found that the rock sample contains mostly dolomite (blue bar) and calcite (green bar)

and minor amounts of the other crystals. The highest peak is eliminated from the

composition because this one indicates aluminum, which is the holder for sample

powders and aluminum does not exist in this rock sample.
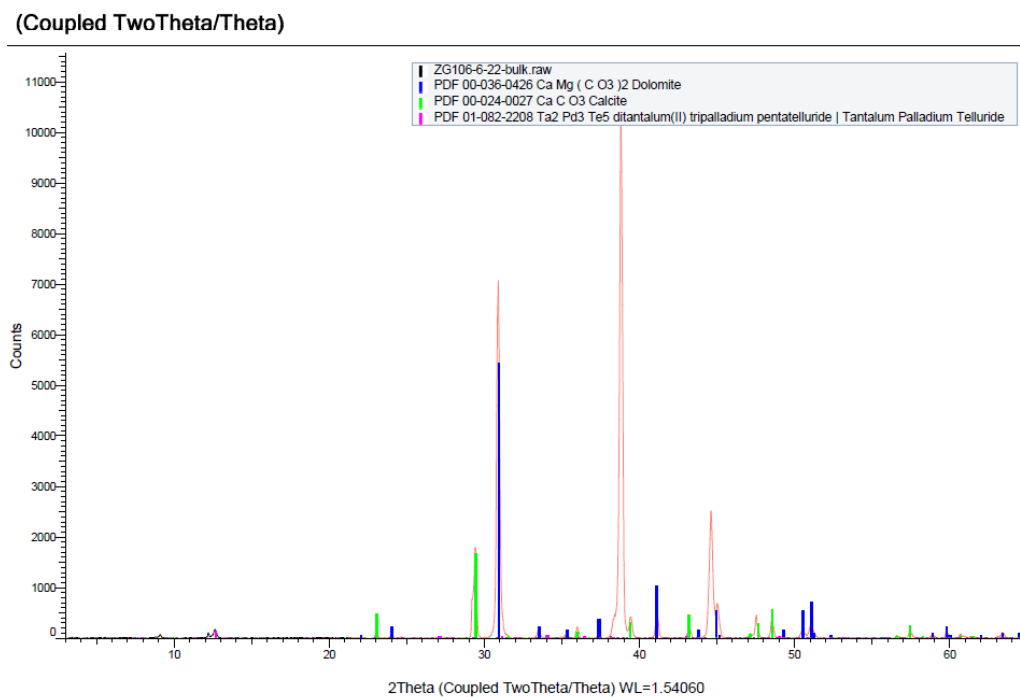
Figure 8. Example XRD result

Nitrogen Adsorption Porosimetry

The fundamental mechanisms of measurement for the nitrogen porosimetry is based on

adsorption theory. Adsorption, like surface tension, is one of the many results of surface

energy. More specifically, atoms are closely bounded together in the internal parts of

solid items due to Van der Waals force. On the contrary, at the surface of these solid

items, one end is not bounded to other atoms. As a result, these surface atoms are much

more reactive to bound free atoms than the rest of the atoms in solid phase. Due to van

der Waals forces of interaction, the surface atoms attract gas or liquids to balance the

atomic forces. As the pressure increases, the adsorption effect will be stronger as

displayed in Figure 9. Powdered rock particles are never perfectly spherical in lab,

instead the rock powder surfaces are rugged with tiny hollows like Figure 9. In this

nitrogen
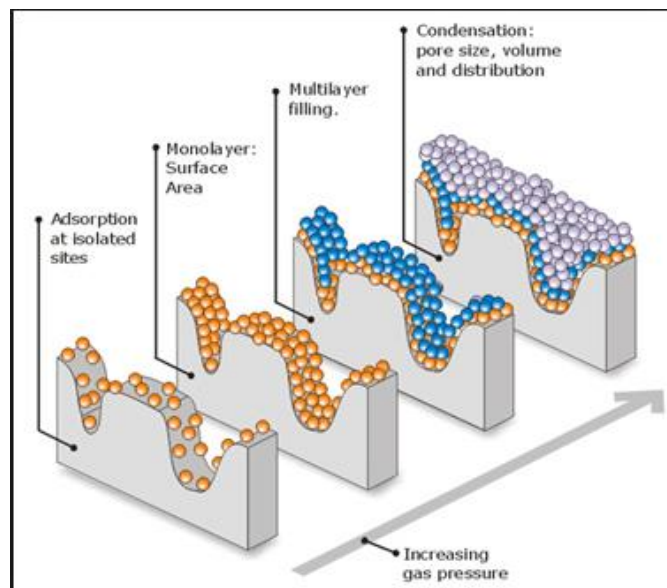
Figure 9. Adsorption of free molecule to a solid surface. Reprinted from Gas Adsorption Theory (2008).

adsorption experiment, rock powders is placed in vacuum environment before nitrogen injection. Nitrogen is injected into the vacuum system dose by dose, each dose of gaseous nitrogen is about 1-3 mmHg. As the pressure increases, more gas is adsorbed onto the rock powder surface until saturation. The amount of gas injected is measured at saturation pressure, which is the micro-pore volume for this rock sample.

The instruments being used in this experiments consists of two parts, SmartVac Prep and 3-Flex Surface Characterization Analyzer, are Micromeritics® company product. The reason we chose these two instruments is because 3-Flex captures both micro-pores (with size less than 2 nm) and meso-pores (with sizes less than 50 nm) better than the other instruments. In other words, any pore that has a diameter of 50nm will be perfectly captured. Nonetheless, during the experiment we observed that 3-Flex not only captures micro and meso pores but also captures relatively larger pores up to about 250nm (equal to 0.25 microns) in size, which is of great benefit to the whole project.

Part 1. Sample Preparation

Sample preparation uses the lab instrument names "SmartVac Prep". In this part of the experiment, the sample is heated up to reservoir temperature (here 80^OC is used for Tarim basin), vacuumed and filled with nitrogen to remove the contaminants usually composed of water, nitrogen and carbon dioxide. These contaminants, as discussed in the previous section, are adsorbed to the surface of rock powders. If contaminants were not removed, the experiment results would be largely impacted and low in accuracy. This part is also referred to as "sample cleaning". Figure 10 shows the SmartVac Prep

instrument. Rock powders are put into the test tubes and then the test tubes are connected to the main instrument. The gray heating pad is then used to cover the bottom part of the test tube and later starts heating to desired temperature. In short, SmartVac Prep heats and vacuums the rock powders, which cleans and prepares the powders for next step.

Part 2. Nitrogen Adsorption Experiment

After being cleaned, the rock sample is well-conditioned for nitrogen adsorption experiment. The test tube with sample will be removed from SmartVac Prep and moved to 3-Flex Surface-pore Characterization Analyzer, where nitrogen adsorption takes place. Three tests would run simultaneously. As shown in Figure 11, the test tube is screwed to the upper part of the instrument. The cylindrical dewar filled with liquid nitrogen and lifted to the same level

Figure 10. SmartVac Prep is a component of the nitrogen adsorption porosimeter. Reprinted from Smart VacPrep Gas Adsorption Sample Preparation Device (2014).

of test tubes during experiment. Thus test tubes are immersed in liquid nitrogen to cool

to cryogenic condition. An adsorptive gas (nitrogen in this experiment) is dosed to the

rock powders in controlled increments. Pressure is equilibrated and adsorption quantity

is calculated after each step of dosing increment. Figure 12 shows the details of such

pressure and adsorption quantity changes. X-axis indicates the ratio of actual pressure

(P) and saturated pressure (Po). From left to right on the x-axis the relative pressure

increases, which could be simply considered to be the increase of actual pressure. Y-axis

gives the absolute cumulative quantity adsorbed in cc per gram of rock powder. The

intuitional observation from Figure 12 is that the adsorbed nitrogen volume increases as

the pressure escalates. The isotherm graph is the foundation for

Figure 11. 3-Flex Surface Characterization Analyzer. Reprinted from 3Flex

Surface Characterization Analyzer (2014).
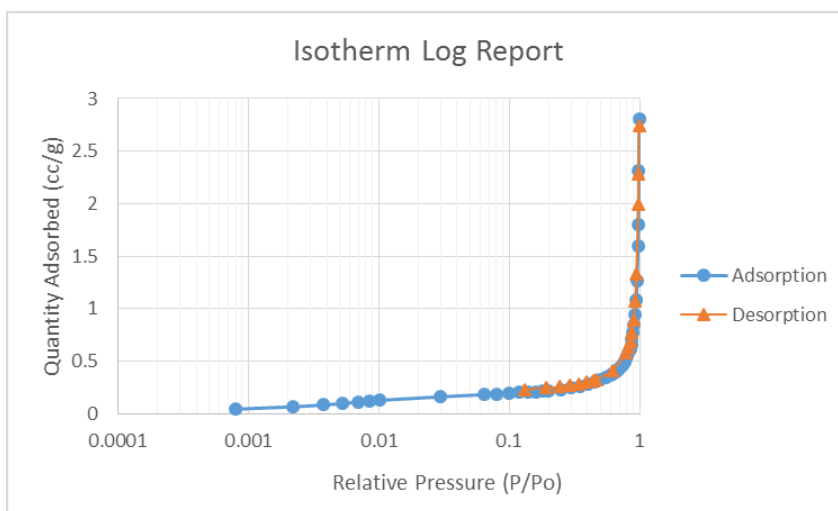
Figure 12. Isotherm graph from 3-Flex (example)

more advanced calculations and analyses from 3-Flex. Based on the isotherm report, more interactive reports could be calculated using different analysis techniques. BET surface area, Langmuir surface area and DFT pore size are the three main analyses utilized with the Tarim samples. More details about these model will be given because they are the ones used in prediction the surface area, pore size distribution and micro-porosity.

Analytical methods, such as Brunauer, Emmett and Teller (BET), Langmuir, Barret-Joyner-Halenda (BJH), etc. have been previously applied for the pores size analysis. However, only the results based on Density-Functional Theory (DFT) analysis are reported here. This is because DFT method accurately captures small pores with the size of less than 200 nm (Adesida 2011). DFT model consists of an empty pore governed by two parallel walls with a distance H. The pore is considered open and immersed in a single adsorptive fluid at a fixed temperature and pressure. In our experiments, nitrogen

20

has been used as the fluid. The fluid responds to the walls and reaches an equilibrium condition where chemical potential at every point equals the chemical potential of the bulk. Such model could be numerically expressed as:

$$Q(p) = \int dH \, q(p, H) \, f(H) \dots \dots Eq(1)$$

Where

Q(p) = the quantity adsorbed at pressure, p, in the experiment,

q(p,H) = the quantity adsorbed per unit area at the same pressure, p, in an ideal pore of size H, and

f(H) = the total area of pores of size H in the sample.

The widely-accepted International Union of Pure and Applied Chemistry (IUPAC) classification has been used and these small pores are grouped as follows: micro-pores with the size of less than 2 nm, meso-pores with the size of 2-50 nm, and macro-pores with the size of larger than 50 nm.

The most significant result DFT provides is the incremental pore volume distribution (Figure 13). Incremental pore volume (y-axis) refers to specific volume at that pore width. For example, assuming pore width is 10 nm, the corresponding incremental pore volume is 0.00004 cc/g. That is, taking all pores that have diameters of 10 nm, add up their volumes and the outcome will be 0.00004 cc/g. The first couple of points are lumped together since the pore size is too small to be captured.

The cumulative pore volume graph (Figure 14) indicates cumulative interconnected pore volume in total when reaching a certain pore width. Assuming pore width equals 10 nm again, the corresponding cumulative pore volume is now about 0.00046cc/g, demonstrating that by adding up all volumes of pores whose widths equal or smaller than 10nm, the volume will be 0.00046 cc/g. Moreover, the rightmost point on Figure 14 reads about 0.004 cc/g (0.00398 cc/g if read from data table), which is the ultimate pore volume of what 3-Flex captured based on all the pores accessed. By multiplying the cumulative pore volume and rock density from XRD results, the ratio of pore volume and grain volume is obtained. If we take one step further, the porosity can be calculated. For example, assuming the rock density is 2.71 g/cc. Therefore $V_{pore}/V_{mineral}$=0.00398 cc/g*2.71 g/cc=0.0108. Moreover, the porosity contribution by pores smaller than 250 nm is 0.0108/1.0108=0.0107.
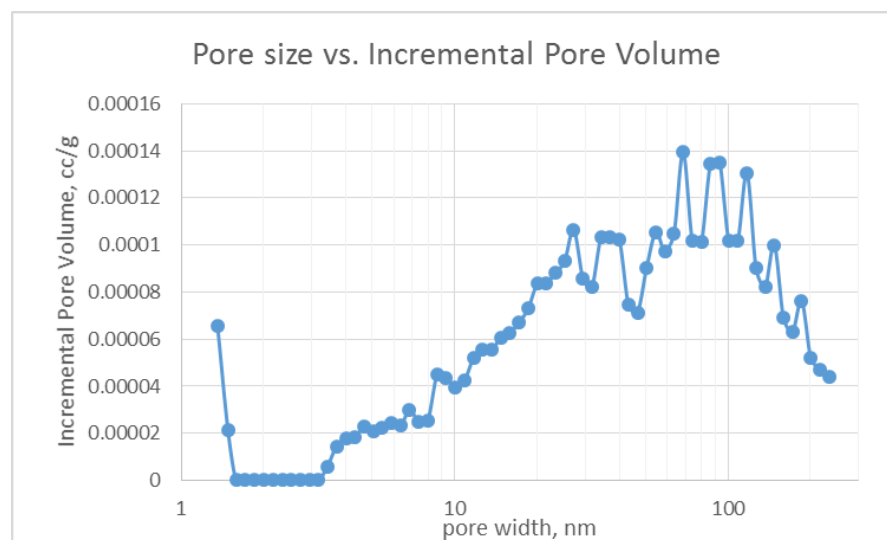

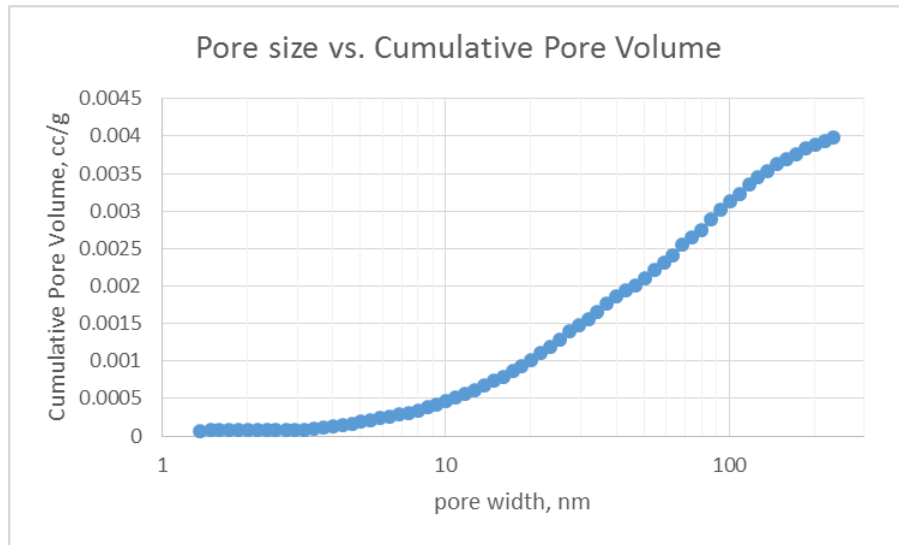**Figure 13. Example pore width vs. incremental pore volume using DFT analysis**

Figure 14. Example pore width vs. cumulative pore volume using DFT analysis

MATRIX COMPONENTS

Matrix components were studied using thin section analysis, SEM image and XRD interpretations. The physics behind these three common tools was introduced in last section. This section will focus on the applications of these tools. Thin sections were taken in a commercial laboratory in China and sent to us for this project. Table 1 shows the total of eight thin section images from the samples taken within the pay zone of well A. All of the images show that the reservoir has experienced high levels of diagenesis. Original pores in the matrix have been filled with calcite. Pressure solution seams (seams formed under high pressure due to dissolution of some rock particles) are present in most images, which indicates a high-pressure environment. Algae and bird's eye structures are present which indicates a tidal-related sedimentary environment and with the geological setting described in the in last section. Bird's eye structures are lensoid pores that are bigger than normal intergranular pores, and may be filled with cement. Lastly, and most importantly, no voids were detected in the images that we can associate with a pore, a pore-throat or a crack. Although in the last two images in Table 1, the description provided by the commercial lab indicated bird-eye structure is present, no pore could be clearly seen in any of these images. Therefore, we think the absence of pores in thin section images might be due to low magnification. As a result, we used a higher magnification instrument from SEM images.
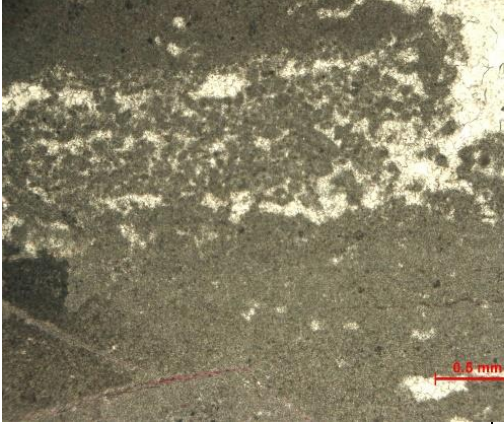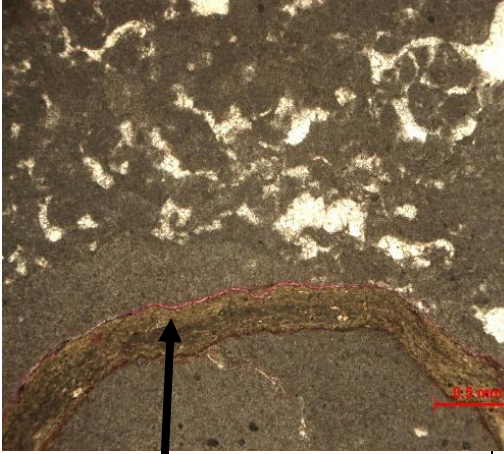
Thin section image	Depth (m)	Description
	6080.62	Layered clotted limestone- Rock matrix has been cemented together. Some lime muds are clotted, pore spaces between clots are cemented by calcite. Part lime muds are stromatolites. Pore spaces between layers are cemented by calcite. Pressure solution styolites co-exist with interlayer pores. Muds stay inside pressolution seam.
Shell fragment	6080.84	Layered clotted limestone- Rock matrix has been cemented. Irregular clots have been observed due to algae's activity. Pore spaces between clots have been cemented by calcite.

Table 1. Well A thin section description

Thin section image	Depth (m)	Description
		Pore spaces between layers (not continuous) are cemented by calcite. Some lime muds are linearly-distributed. One side of shell fragment is uniform lime muds. Inside the shell fragment is sericites and chlorites.
Pressure solution styolite	6081.03	Layered clotted limestone-Rock matrix is cemented. Irregular clots have been observed due to algae's activity. Pressure solution styolite shows an irregular shape with sericite inside. Uniform lime muds and clotted lime muds evenly distributed.

Table 1 (continued). Well A thin section description
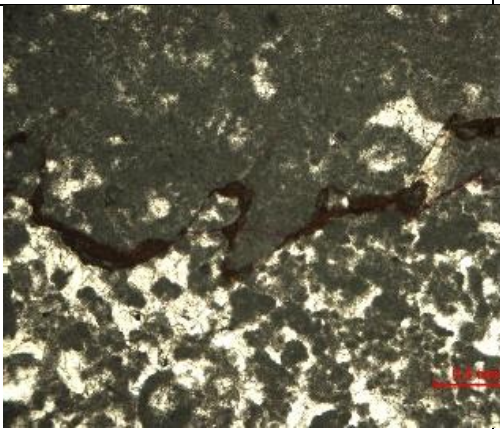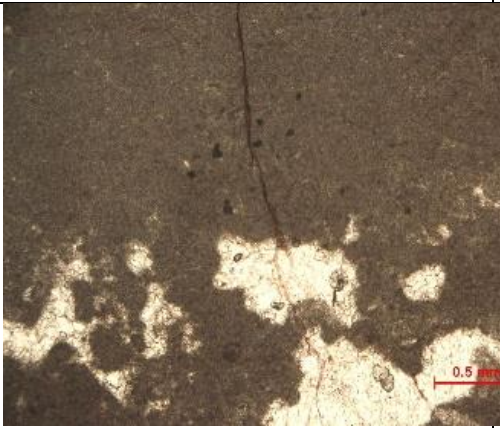
Thin section image	Depth (m)	Description
	6081.21	Layered, clotted limestone- Matrix is cemented. Irregular clots have been observed due to algae's activity. Pore spaces cemented by calcite. Uniform lime muds layer and clotted lime muds layer alternatively distributed.
	6081.56	Layered clotted limestone- Matrix is cemented. Some lime muds are irregular clotted. Pore spaces cemented by calcite. Uniform lime muds layer and clotted lime muds layer alternatively distributed.

Table 1(continued). Well A thin section description
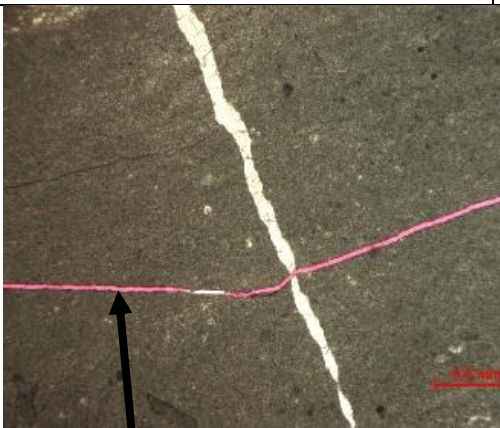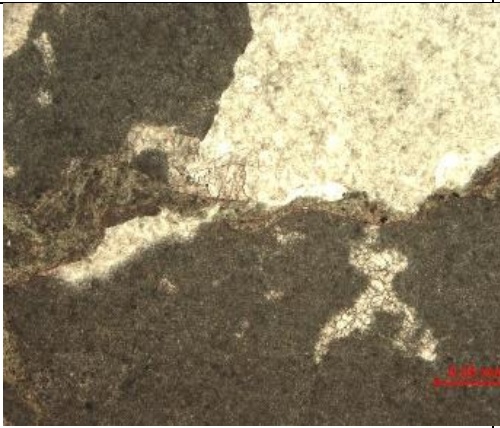
Thin section image	Depth (m)	Description
fracture	6082.19	Micrite limestone- Rock composed of lime muds with uniform structure. Bird's eye structure is seen along laminas 6% (cemented by calcite). Pressolution seam is zig-zag shaped parallel to lamina. Interlayer pores are cemented by calcite.
	6082.68	Micritic limestone- Rock composed of lime muds with relatively simple composition and structure. Different sizes and shapes bird-eye pores exist (8%). The rest part is cemented by calcite.

Table 1 (continued). Well A thin section description
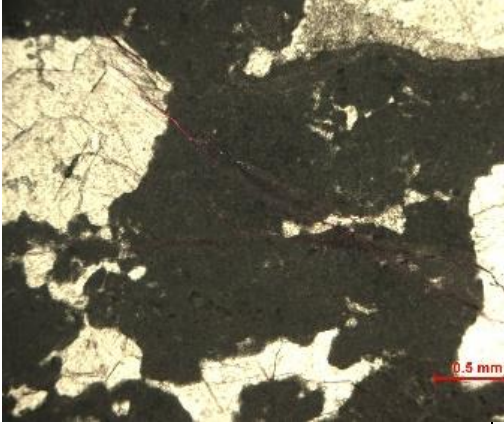
Thin section image	Depth (m)	Description
	6082.73	Micritic limestone with bird-eye pores- Rock composed of micrite calcite. Many bird's eye pores with different sizes and shapes orientated in the direction of long axis. The rest parts are cemented by calcite.

Table 1 (continued). Well A thin section description

SEM image magnifications are between 10 and 20000 and zoomed in to an even smaller surface area compared to thin section. Figure 15(a) shows micro-fractures, which is the darker shaded area in upper left corner, could be clearly observed while in microscopic thin section images these micro-fractures are those tiny pink lines which are almost impossible to detect. Figure 15(b) magnification is 1000x (the indicated length on lower right corner is 50 μm), and thus the surface area in Figure 15(b) is 1/16 of Figure 15(a). In Figure 15(b) we observed several small pores, which are indicated as the darker spots. Also, the surface of matrix is not even; these tiny fractures and unconformities are very important for tight formation pore size distribution analysis, because the pores beside these fractures and unconformities add up to a significant amount of volume of pore space. More information will be provided in next section.

When the SEM image is further zoom in to an even smaller area, for which the magnification is 6500x (normal scale length on lower right corner is 5 μm), the SEM image shows a porous matrix with the pore diameter ranging from about 600 nm up to more than 2 μm as displayed in Figure 15(c). Not until this image could we believe that this matrix could serve as a good reservoir because at smaller magnifications pores are barely seen. Figure 15(d) magnifies the surface at 80,000x (the normal length on lower
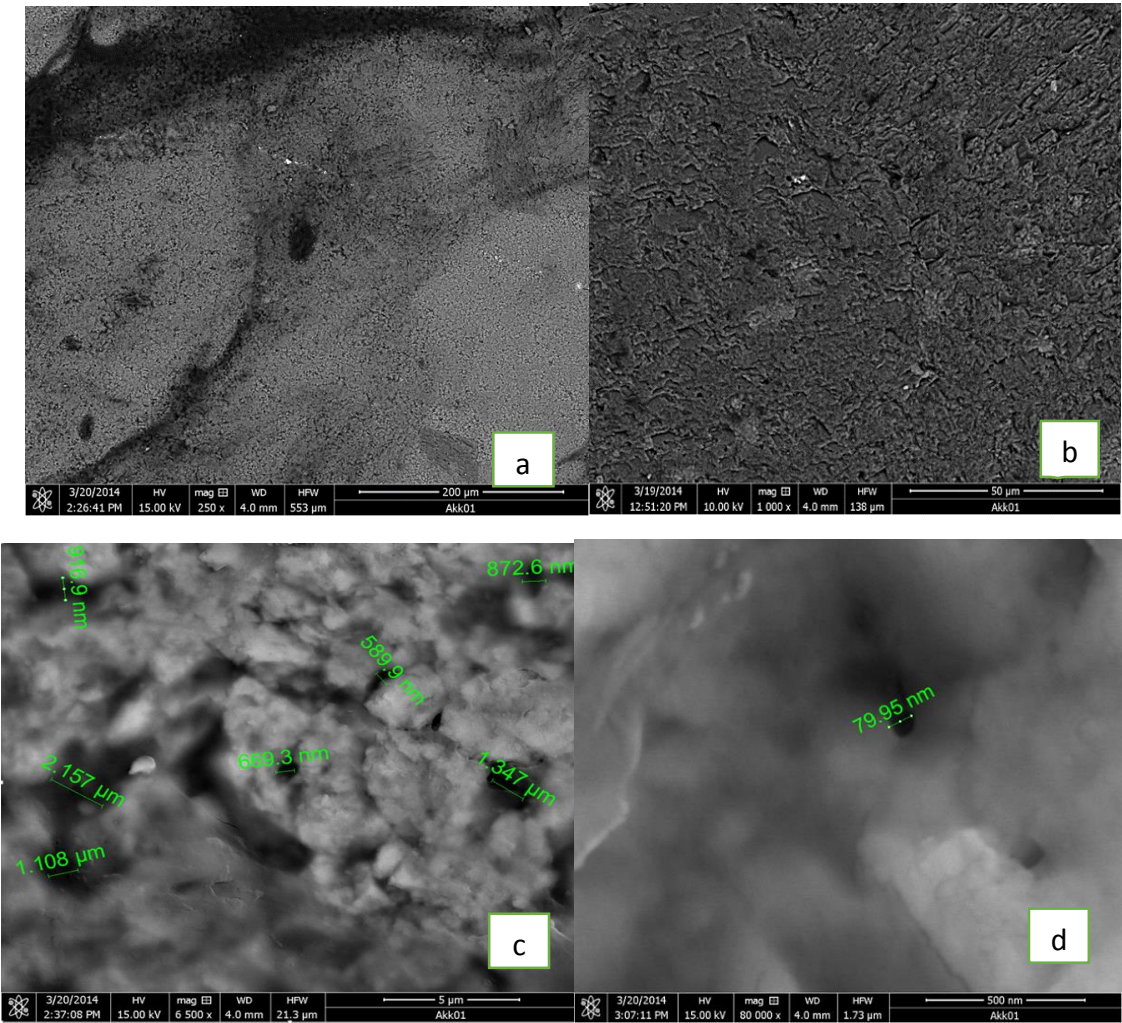
Figure 15. SEM images at different magnifications

right corner is 500 nm). Conversely to our expectation, when adjusting the magnification from Figure 15(c) to (d), not as much pores have been observed. Such fact indicates that in this specific area being tested, magnification of 6500x most clearly captures the pores, demonstrating the vast majority of pores have diameter between 600 nm to 2 μm or the same order of magnitude. Also in Figure 15(d) the image is vague and not clear enough compared to previous pictures, this suggests the SEM instrument has reached the highest magnification and could not zoom in any more under the current setting.

The XRD results for the cores from the well A are summarized in Table 2. The cores have almost identical mineral composition, being consisted of 24% calcite and 75% dolomite, plus a small amount of kaolinite. In general the XRD analyses indicates that the formation composition is very simple and homogeneous, which matches the nitrogen porosimetry results that will be discussed later. Recall Figure 8, which is the XRD outcome for well A 5-1/22 and the exact components are listed below in Table 2.

Sample	Calcite	Kaolinite	Dolomite	Density, g/cc
well A 5-1/22	23.52%	0.27%	76.21%	2.830
well A 5-5/22	24.06%	1.71%	74.23%	2.827

Table 2. XRD results for well A

PORE SIZE DISTRIBUTION

Pore size analysis using DFT was performed for samples from two core plugs from the well A: well A 5-1/22 and well A 5-5/22.

Based on the DFT analysis, only one type of formation is identified in the well. Figures 16 and 17 show typical behaviors of this type of formation in well A. The cumulative pore volume contribution in this sample for well A 5-1/22 core exceeds 0.004 cc per gram. The incremental pore size distribution plot shows that the pore volume for the same sample is due to meso- and macro-pores with sizes mainly in between 10-200 nm. Nano-scale pores with sizes less than 10 nm also exist, although their contribution to the total pore volume nearly negligible. In addition, it is possible that there are pores greater than 200 nm, but DFT method using nitrogen adsorption data cannot capture those relatively large pores.

The cumulative pore volume from small pores for well A is around 0.0042 cc/g of rock sample. In macro-pore region, the average contribution for each pore width is about 0.00008 to 0.00012 cc per gram of rock. The other graphs for well A 5-5/22 are given to at the end of this section.

Summary figures for well A are plotted together in Figures 18 and 19. There are only two samples for this formation. The average estimations of two lines are plotted in red thick lines, both in cumulative and incremental distributions. Figure 18 and Figure 19 display cumulative and incremental distribution figures for this type of formation. In general, the trends for each line are very similar, so that the average curves look quite

comparable to other curves in the figures. Micro- pores contribute little to total pore volume while meso- and macro-pores are the main portions that make up the pore structure of small pores. As a result, the average curve keep every information in but does not eliminate noise (the zig-zag shaped average line in Figure 19) and gives a smooth line (especially incremental curve), which is what we expected theoretically. Nonetheless, since there are only two rock samples available for this formation, and both show strong similarities, the zig-zag shape in incremental pore volume distribution could be treated as the way it looks like and no more smoothing is needed. The average values of pore volume will be the input for further analyses, software simulation or modeling, for instance. Because the average curve could represent these two lines, the results from simulation or modeling software should be accurate and reliable. The averaged cumulative pore volume is about 0.0042 cc per gram of rock for all small pores.
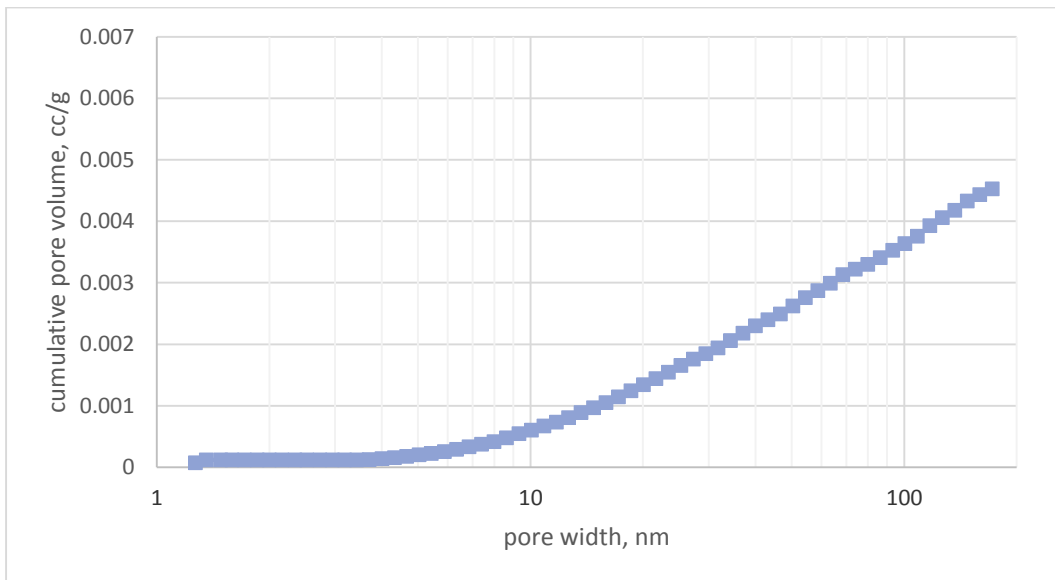
Figure 16. Cumulative pore volume vs. pore width for well A 5-1/22
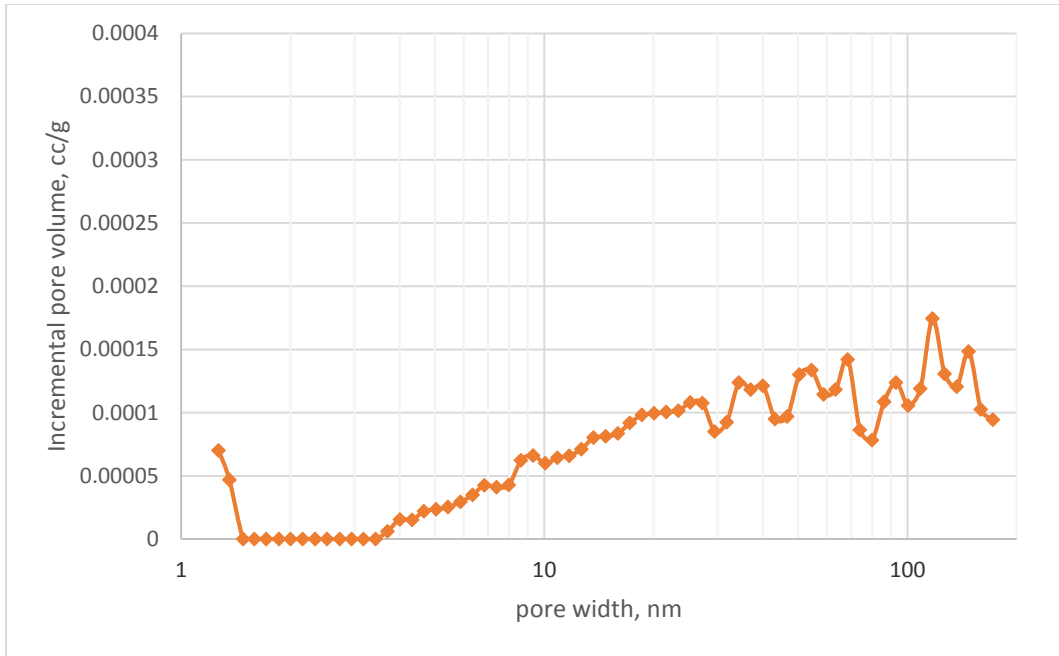
Figure 17. Incremental pore volume vs. pore width for well A 5-1/22
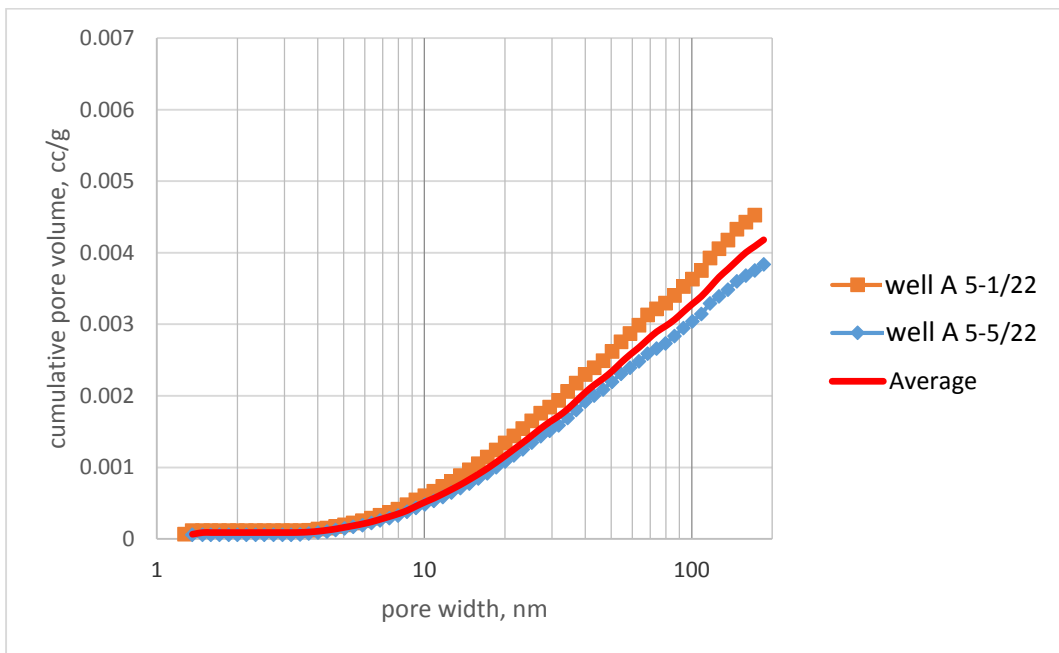
Figure 18. Cumulative pore volume vs. pore width for well A
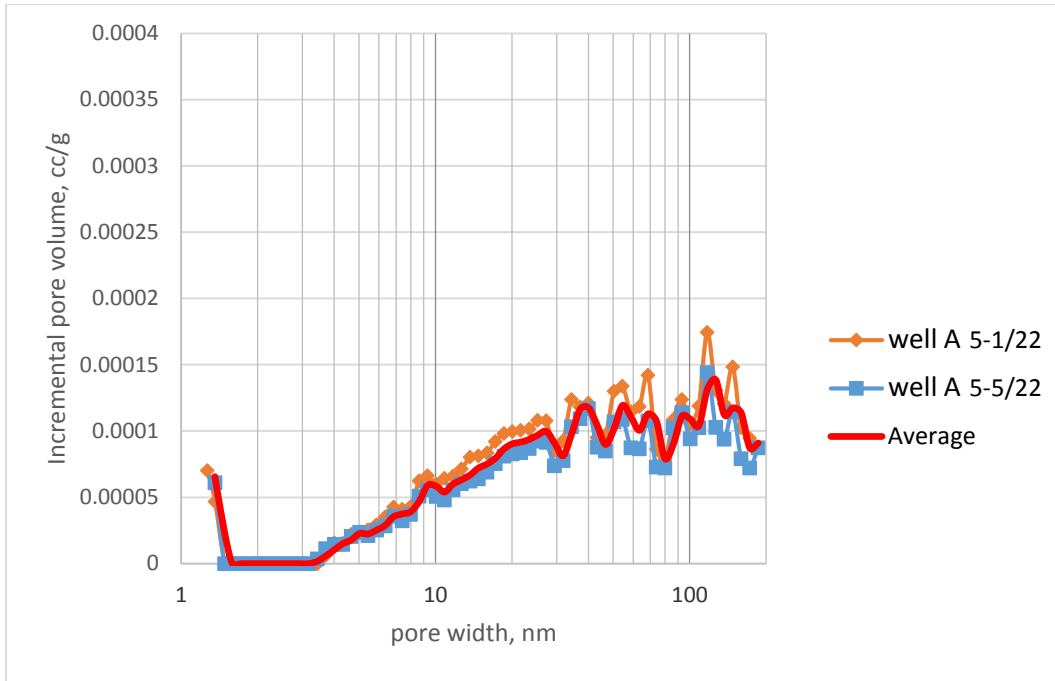
Figure 19. Incremental pore volume vs. pore width for well A

In this section, effective pore size, small-pore porosity and small-pore volume contribution to total pore volume are discussed. These calculations are based on the nitrogen porosimetry and XRD data. Also, helium porosity values, which have previously been measured independently in the Tarim group, are used in this section. The helium porosity values are given in Table 3.

Sample	Helium porosity
well A 1/22	0.025
well A 5/22	0.027

Table 3. Helium porosity for well A

The first calculation is the computation of effective pore size, which follows equation 2:

Thus, the following computations were completed:

$$\text{Effective Pore Width} = \frac{\sum(Pore\ Width \times Incremental\ Volume)}{\sum(Incremental\ Volume)} \dots \text{eq}(2)$$

$$\text{Effective Pore Width (Well A 5} - 1/22) = \frac{0.25587}{0.004525} = 56.54\ \text{nm}$$

$$\text{Effective Pore Width (Well A 5} - 5/22) = \frac{0.227082}{0.00384} = 59.14\ \text{nm}$$

$$\text{Effective Pore Width (Well A average)} = \frac{0.241767}{0.004182} = 57.81\ \text{nm}$$

The second calculation is the estimation of the small-pore porosity, i.e., the small pore contribution to the measured pore volume. In this scenario, absolute porosities are calculated excluding the pores larger than 200 nm. Hence, the total pore volume is purely contributed by the pores that the nitrogen adsorption porosimeter could capture. This assumption is important as well as helpful in pore structure modeling. The average small-pore porosity is estimated using Equation 3. In this approach the grain density is also required, which is measured for each sample. The average porosity is computed by taking the arithmetic average of two porosities.

$$\text{Porosity} = \frac{V_{pore}}{V_{bulk}} = \frac{V_{pore}}{V_{pore} + V_{grain}} = \frac{V_{pore}/V_{grain}}{1 + V_{pore}/V_{grain}} \dots \dots \text{eq}(3)$$

$$\text{Small Pore Porosity(Well A 5} - 1/22) = \frac{0.00453/0.35336}{1 + 0.00453/0.35336} = 1.27\%$$

$$\text{Small Pore Porosity(Well A 5} - 5/22) = \frac{0.00384/0.35373}{1 + 0.00384/0.35373} = 1.09\%$$

$$\text{Small Pore Porosity(Well A average)} = \frac{1.27\% + 1.09\%}{2} = 1.18\%$$

After obtaining the absolute porosity of the small pores, ratio of the small pores in the

total pore volume was estimated, which is the most important calculation in determining

which type of pore-network modeling to be chosen in reservoir modeling software. The

ratio of smaller pore contribution is simply obtained by Equation 4 below:

$$\text{Small Pore Contribution Ratio} = \frac{\text{Small Pore Porosity}}{\text{Helium Porosity}} \dots\dots eq(4)$$

$$\text{Small Pore Contribution Ratio(Well A 5} - 1/22) = \frac{1.27\%}{2.55\%} = 49.8\%$$

$$\text{Small Pore Contribution Ratio(Well A 5} - 5/22) = \frac{1.09\%}{2.74\%} = 39.8\%$$

$$\text{Small Pore Contribution Ratio(Well A average)} = \frac{49.8\% + 39.8\%}{2} = 44.8\%$$

Where helium porosity, which has been measured before, is shown in Table 3. Again the

arithmetic average of two samples are calculated and used as the average porosity. The

calculations indicate that in well A, small pores contribute more than 40% of the total

pore volume in average. Therefore, if reservoir modeling is applied to simulate this well,

dual porosity model has to be chosen. Otherwise more than 40% of the pore volume is

not correctly treated. Also, due to the fact that small pores take up more than 40% of the

total pore volume, well A should behave somewhat like an ultra-tight unconventional

formation.

RESULTS FROM OTHER WELLS

Results for Well B

Summary figures for well B are plotted together in Figure 20 and Figure 21. There are three samples for this formation. The average estimations of three lines are plotted in red thick lines, both in cumulative and incremental distributions.

Figure 20 and Figure 21 display cumulative and incremental distributions for the formation. The trends for each line are very similar to each other so that the average curves look quite comparable to other curves in the figures. As a result, the average curve keep every information in but does not eliminate noise (the zig-zag shaped average line in Figure 21) and gives a smooth line (especially incremental curve), which is what we expected theoretically. Nonetheless, since there are only three rock samples available for this type of formation, and all of them show strong similarities, the zig-zag shape in incremental pore volume distribution could be treated as the way it looks like and no more smoothing is needed. The average values of pore volume will be the input for further analyses, software simulation or modeling, for instance. Because the average curve could represent all three lines, the results from simulation or modeling software should be accurate and reliable. The averaged cumulative pore volume is about 0.005 cc per gram of rock for all small pores.
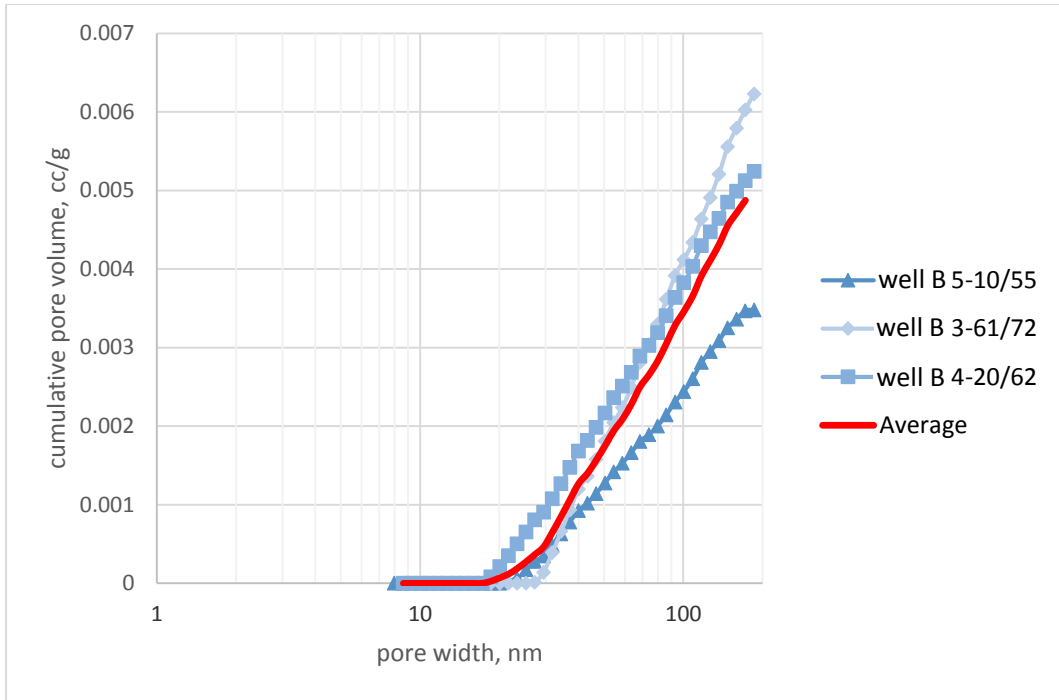
Figure 20. Cumulative pore volume vs. pore width for well B
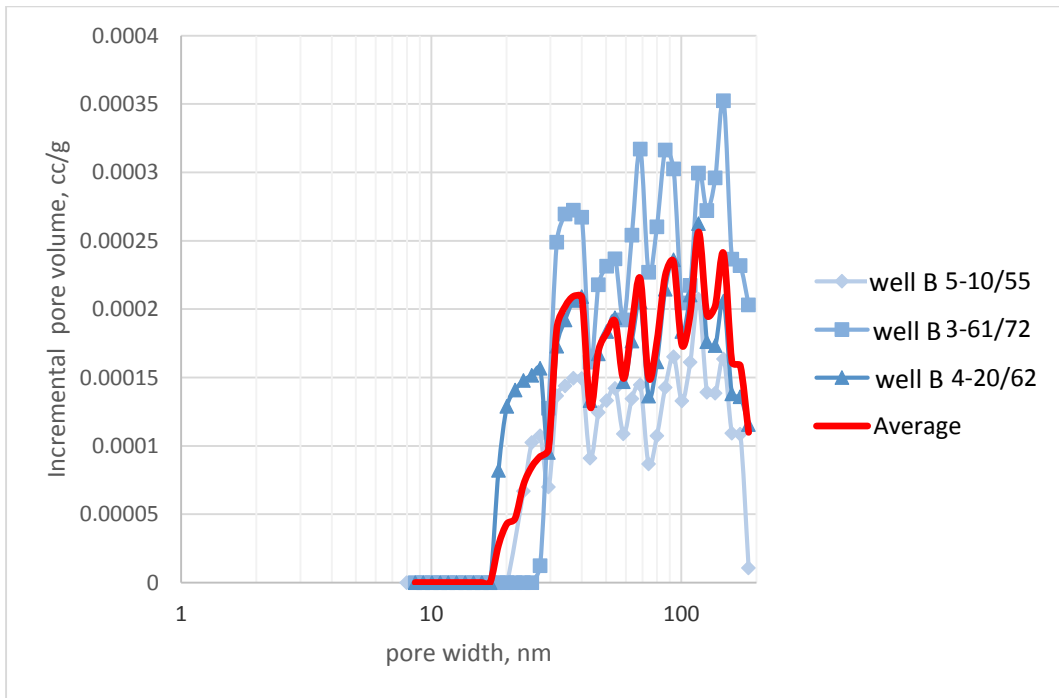
Figure 21. Incremental pore volume vs. pore width for well B

39

The XRD results for the cores from the well B are summarized in Table 4. The cores have almost identical mineralogy compositions, being consisted of nearly pure calcite, except for the existence of a small amount of kaolinite and lizardite in the core well B 4 20/62. In general the XRD experiment outcomes indicate that the formation compositions are very simple and homogeneous, which match the nitrogen porosimetry results that all three samples display similar pore structures.

Rock sample	calcite	kaolinite	lizardite	Density, g/cc
well B 3 -61/72	100%	---	---	2.710
well B 4-20/62	94.11%	2.75%	3.13%	2.702
well B 5-10/55	100%	---	---	2.710

Table 4. XRD results for well B

Effective pore size, small-pore porosity and small-pore volume contribution to total pore volume are summarized below. These calculations are based on the nitrogen porosimetry and XRD data. Also, helium porosity values, which have previously been measured independently in the Tarim group, are used in this section. The helium porosity values are given in Table 5.

Rock sample	Helium porosity
well B 3 -61/72	0.01704
well B 4-20/62	0.01437
well B 5-10/55	0.0175

Table 5. Helium porosity for well B

The effective pore width results are:

$$\text{Effective Pore Width (Well B 3} - 61/72) \ = \frac{5.47515}{0.06229} = 87.90 \text{ nm}$$

$$\text{Effective Pore Width (Well B 4} - 20/62) \ = \frac{3.95749}{0.05241} = 75.51 \text{ nm}$$

$$\text{Effective Pore Width (Well B 5} - 10/55) \ = \frac{2.75627}{0.03479} = 79.24 \text{ nm}$$

$$\text{Effective Pore Width (Well B average)} \ = \frac{0.406279}{0.0049832} = 81.54 \text{ nm}$$

The small pore absolute porosities are:

$$\text{Small Pore Porosity(Well B 3} - 61/72) \ = \frac{\frac{0.00623}{0.36900}}{1 + \frac{0.00623}{0.36900}} = 1.66\%$$

$$\text{Small Pore Porosity(Well B 4} - 20/62) \ = \frac{\frac{0.00524}{0.37010}}{1 + \frac{0.00524}{0.37010}} = 1.40\%$$

$$\text{Small Pore Porosity(Well B 5} - 10/55) \ = \frac{\frac{0.00348}{0.36900}}{1 + \frac{0.00348}{0.36900}} = 0.934\%$$

$$\text{Small Pore Porosity(Well B average)} = \frac{1.66\% + 1.40\% + 0.934\%}{3} = 1.33\%$$

After obtaining the absolute porosity of the small pores, ratio of the small pores in the

total pore volume were estimated, which is the most important calculation in

determining which type of pore-network modeling to be chosen in reservoir modeling

software. The ratios of smaller pore contribution are:

$$\text{Small Pore Contribution Ratio(Well B } 3-61/72) = \frac{1.66\%}{1.70\%} = 97.7\%$$

$$\text{Small Pore Contribution Ratio(Well B } 4-20/62) = \frac{1.40\%}{1.44\%} = 97.2\%$$

$$\text{Small Pore Contribution Ratio(Well B } 5-10/55) = \frac{0.934\%}{1.75\%} = 53.4\%$$

$$\text{Small Pore Contribution Ratio(Well B average)} = \frac{97.7\% + 97.2\% + 53.4\%}{3}$$

$$= 82.8\%$$

Helium porosity for well B is not measured exactly at the point where the nitrogen porosimetry is carried out, but well B is very homogeneous and therefore some nearby rock helium porosity is used. The average contribution ratio is computed by taking the arithmetic average of three porosities. Those helium porosities are shown in Table 5.

The calculations indicate that in well B formation, small pores contribute over 80% of the total pore volume in average. Therefore, if reservoir modeling is applied to simulate this well, dual porosity model has to be chosen otherwise more than 80 % of the pore volume is not correctly treated. Also, due to the fact that small pores take up a large amount of total pore volume, well B should behave very much like some other carbonate unconventional formations, such as Bakken.

Results for Well C

The pore size analysis was performed by using four core plugs from the well C: well C 1-29/57, well C 1-18/57, well C 3-62/66 and well C 3-62/66. Based on the DFT analysis,

42

two pore types are identified in well C: Pore Type I and Pore Type II. Here Pore Type I refers to a complex pore structure system, where pore sizes vary from large to small and both large and small pores are important in total pore volume construction. On the other hand, Pore Type II is defined to be a simple pore structure system where pore sizes are relatively uniform and large, with little small pore in the total pore structure system. Figure 22 and 23 show behavior of Type I formation in well C. The cumulative pore volume contribution of Pore Type I is larger than 0.003 cc per gram. The incremental pore size distribution plot shows that the pore volume for the same sample is mainly between 10-200 nm, which are considered to be meso- and macro-pores. Some nano-scale pores with sizes less than 10 nm also exist, although we find their contribution to the total pore volume almost negligible. In addition, it is possible that there are pores with the size of larger than 200 nm, but DFT method using nitrogen adsorption data cannot capture those relatively large pores.

The cumulative pore volume from small pores for Type I is around 0.0035 cc per gram of rock sample. In macro- pore region, the average contribution for each pore width is about 0.00008 to 0.0001 cc per gram of rock. Typical Pore Type II cumulative and incremental pore size distribution are plotted in Figure 24 and 25, respectively. These two figures are based on the experimental data for sample well C 1-29/57 and well C 1-18/57. The same plotting scales have been applied to all figures such that the differences in Pore Types I and II are easy to observe. Compared to Pore Type I structure, Pore Type II is acting as a solid block (with no pores) with negligible small pore volume contribution. The pores captured by the porosimeter are below 10 nm, and

completely lack macropores and mesopores with sizes larger than 10 nm. Note that,

although these samples lack small, pores, they may include larger macropores or even
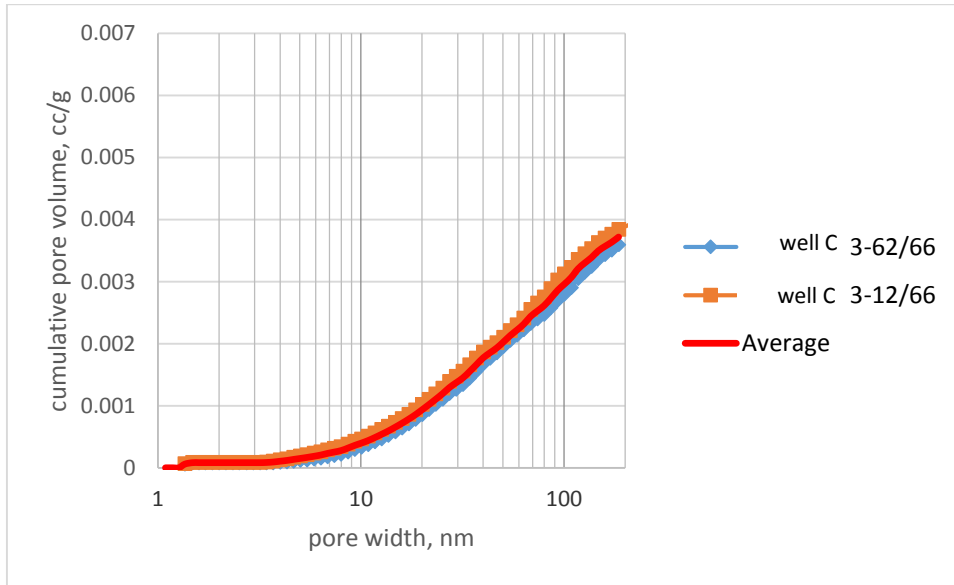
fractures at a larger scale.

Figure 22. Pore Type I cumulative pore volume distribution for well C
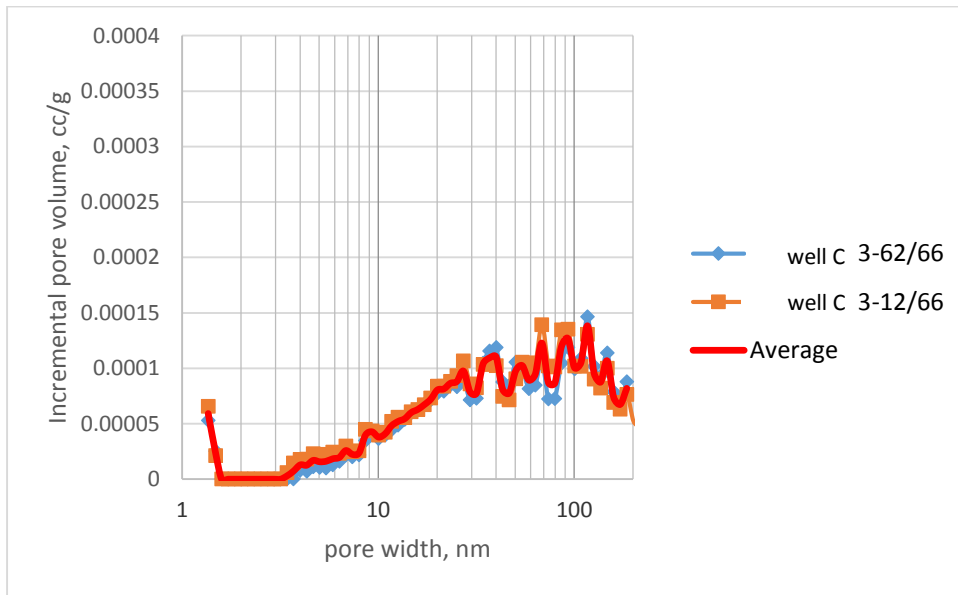

Figure 23. Pore Type I incremental pore volume distribution for well C
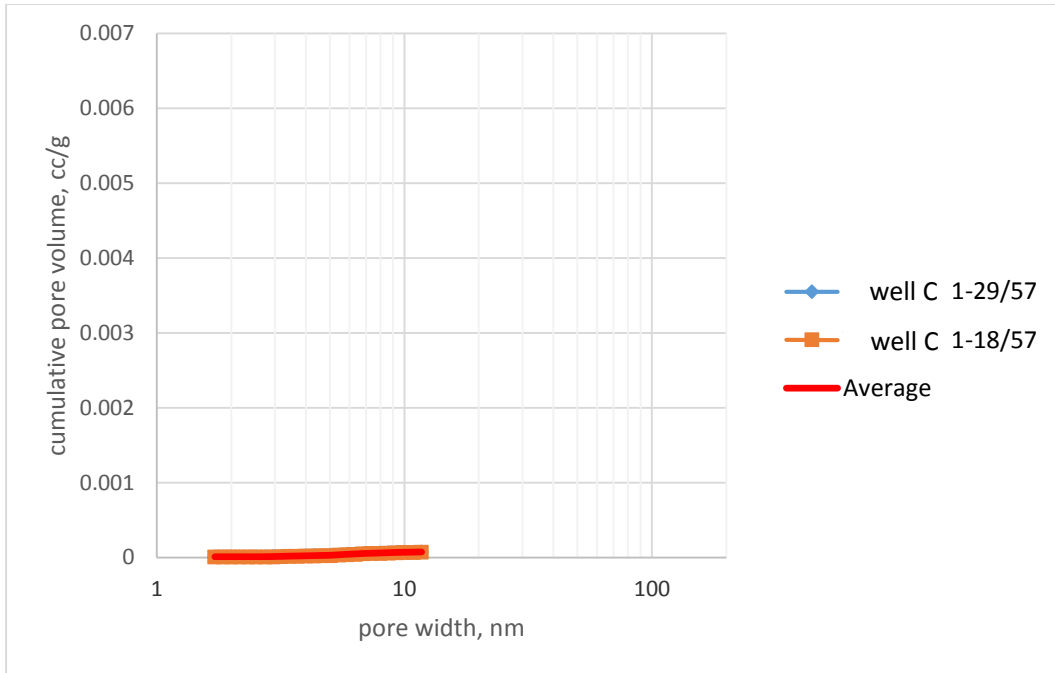
Figure 24. Pore Type II cumulative pore volume distribution for well C
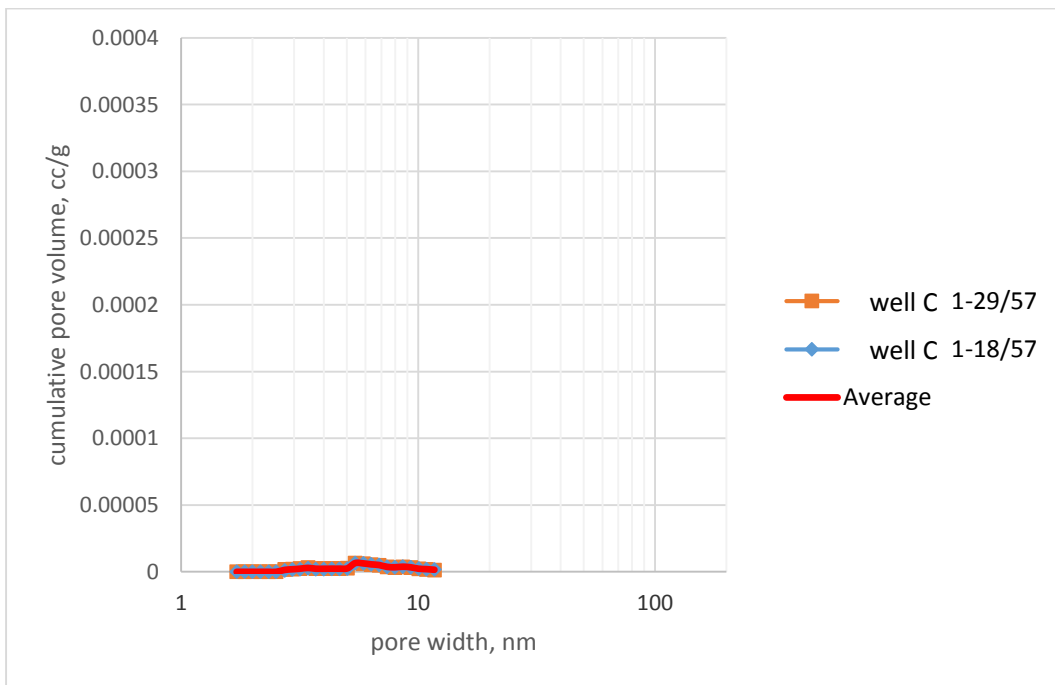
Figure 25. Pore Type II incremental pore volume distribution for well C

The XRD results for the cores from the well C are summarized in Table 6. The measurements are very accurate for the carbonate rocks so that two decimal points are reported. The results show that the samples dominantly include calcite. Formation with Pore Type I structure (well C 3-62/66 and well C 3-12/66) present absolutely the same compositions, pure calcite. Formation with Pore Type II structure (well C 1-29/57 and well C 1-18/57) is mostly calcite, but mixed with small amounts of quartz, dolomite and ankerite. In general, the compositions of the samples are very simple and homogeneous. Based on the compositions, a density value was also calculated for each rock sample.

Sample	Calcite	Dolomite	Quartz	Ankerite	Density, g/cc
well C 3-62/66	100%	---	---	---	2.710
well C 3-12/66	100%	---	---	---	2.710
well C 1-29/57	94.96%	0.77%	3.75%	0.52%	2.711
well C 1-18/57	80.18%	14.93%	3.02%	1.88%	2.743

Table 6. XRD results for well C

The effective pore width results are:

$$\text{Effective Pore Width (Well C 3} - 62/66) \ = \ \frac{0.25670}{0.0039813} = 64.47 \text{ nm}$$

$$\text{Effective Pore Width (Well C 3} - 12/66) \ = \ \frac{0.22527}{0.0035953} = 62.66 \text{ nm}$$

$$\text{Effective Pore Width (Well C 1} - 29/57) \ = \ \frac{0.0003984}{0.00006463181} = 6.164 \text{ nm}$$

$$\text{Effective Pore Width (Well C 1} - 18/57) \ = \ \frac{0.0004066}{0.0000633151} = 6.422 \text{ nm}$$

$$\text{Effective Pore Width (Well C Pore Type I)} \ = \ \frac{0.22551}{0.003567} = 63.22 \text{ nm}$$

$$\text{Effective Pore Width (Well C Pore Type II)} \ = \ \frac{0.0004025}{0.0000639733} = 6.292 \text{ nm}$$

The small pore absolute porosities are:

$$\text{Small Pore Porosity}\left(\text{Well C 3} - \frac{62}{66}\right) = \frac{\frac{0.00360}{0.36900}}{1 + \frac{0.00360}{0.36900}} * 100\% = 0.966\%$$

$$\text{Small Pore Porosity}(\text{Well C 3} - 12/66) = \frac{\frac{0.00398}{0.36900}}{1 + \frac{0.00398}{0.36900}} * 100\% = 1.07\%$$

$$\text{Small Pore Porosity}(\text{Well C 1} - 29/57) = \frac{\frac{0.00008}{0.36887}}{1 + \frac{0.00008}{0.36887}} * 100\% = 0.0217\%$$

$$\text{Small Pore Porosity}(\text{Well C 1} - 18/57) = \frac{\frac{0.00007}{0.36456}}{1 + \frac{0.00007}{0.36456}} * 100\% = 0.0192\%$$

$$\text{Small Pore Porosity}(\text{Well C Pore Type I}) = \frac{0.966\% + 1.07\%}{2} * 100\% = 1.02\%$$

$$\text{Small Pore Porosity}(\text{Well C Pore Type II}) = \frac{0.0217\% + 0.0192\%}{2} * 100\%$$
$$= 0.0205\%$$

After obtaining the absolute porosity of the small pores, ratios of the small pores in the total pore volume were estimated, which is the most important calculation in determining which type of pore-network modeling to be chosen in reservoir modeling software. The ratio of small pore contributions are:

$$\text{Small Pore Contribution Ratio}(\text{Well C 3} - 62/66) = \frac{0.966\%}{2.9\%} = 33.3\%$$

$$\text{Small Pore Contribution Ratio}(\text{Well C 3} - 12/66) = \frac{1.07\%}{3.07\%} = 34.5\%$$

$$\text{Small Pore Contribution Ratio}(\text{Well C 1} - 29/57) = \frac{0.0217\%}{2.63\%} = 0.825\%$$

$$\text{Small Pore Contribution Ratio}(\text{Well C 1} - 18/57) = \frac{0.0192\%}{4.24\%} = 0.453\%$$

$$\text{Small Pore Contribution Ratio(Well C Type I)} = \frac{33.3\% + 34.9\%}{2} = 34.1\%$$

$$\text{Small Pore Contribution Ratio(Well C Type II)} = \frac{0.825\% + 0.453\%}{2} = 0.639\%$$

Also, helium porosity values, which have previously been measured independently, are used in this section. The helium porosity values are given in Table 7.

Sample	Helium Porosity, fraction
well C 3-62/66	2.9%
well C 3-12/66	3.1%
well C 1-29/57	2.6%
well C 1-18/57	4.2%

Table 7. Helium porosity for well C

PERMEABILITY ANALYSIS

The study on relationship between porosity and permeability started decades ago, however, current available outcomes are all based on porosity measured by helium porosimeter or log interpretation. How small pores relate to permeability is a problem yet to solve. Also, discussions on which porosity-permeability calculation is the most accurate method have been going on for decades and seems like two methods that industry agrees on are the Kozeny-Carmen calculation and Coates' method to predict permeability in low-porosity formations.

Besides the calculations based on log interpretations, permeability can also be estimated using Kozeny-Carmen equation. Initially, Kozeny-Carmen equation discusses how fluid flows within a rock matrix. With a little modification, Kozeny-Carmen equation could be used to express the relationship between porosity and permeability. The most important assumption made in this equation is that pore spaces inside a rock matrix are all connected as different capillary tubes, like Figure 26 (a). However, these capillary tubes are not always straight, a more common case is displayed in Figure 26 (b), where the capillary tube, or called the flow path, is curved.
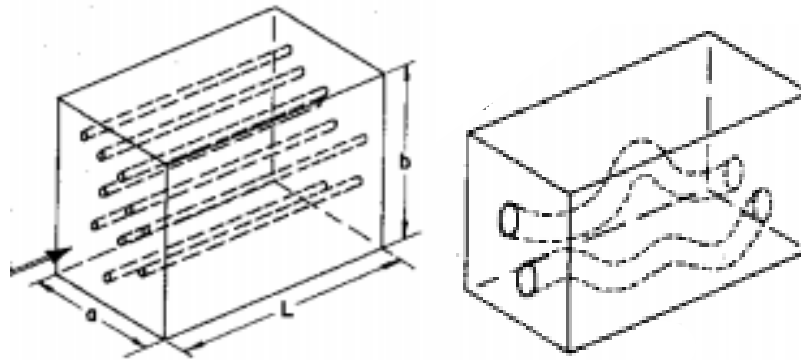
Figure 26 (a) and (b). Kozeny-Carmen assumptions of pore spaces inside a rock matrix. Reprinted from Porosity-Permeability Relationships (2010).

The study of Kozeny-Carmen equation starts from the laminar flow equation in a

circular pipe with radius a in axial coordinates, which is expressed as:

$$\frac{\partial^2 u}{\partial r^2} + \frac{1}{r}\frac{\partial u}{\partial r} = \frac{1}{\mu}\frac{dp}{dx} \ldots \ldots eq(5)$$

Where,

u, μ are the flow velocity and viscosity, respectively.

A general solution to the equation above is:

$$u = \vec{A} + \vec{B}r^2 + \vec{C}lnr \ldots \ldots eq(6)$$

Thus,

$$\frac{\partial u}{\partial r} = 2\vec{C}r + \frac{\vec{C}}{r} \text{ and } \frac{\partial^2 u}{\partial r^2} = 2\vec{C} + \frac{\vec{C}}{r^2} \ldots \ldots eq(7)$$

By substituting these two equation back into eq(*), it is obvious that,

50

$$\vec{B} = \frac{1}{4\mu}\frac{dp}{dx} \dots\dots eq(8)$$

Assuming there is no slippage along the wall, at r=a,

$$u = \vec{A} + \vec{B}r^2 = \vec{A} + \frac{1}{4\mu}\frac{dp}{dx}a^2 = 0 \dots\dots eq(9)$$

Hence,

$$\vec{A} = -\frac{1}{4\mu}\frac{dp}{dx}a^2 \text{ and } u = -\frac{1}{4\mu}\frac{dp}{dx}a^2\left(1 - \frac{r^2}{a^2}\right) \dots\dots eq(10)$$

From the expression of u, the final flow rate could be written as:

$$q = -\frac{\pi a^4}{8\mu}\frac{\Delta p}{l} \dots\dots eq(11)$$

Here, l is the flow length, when encountered with tortuosity such as Figure 26(b), l equals to L*τ where L is the matrix length and τ the tortuosity factor. Assuming there exists N capillary tubes inside a matrix, the total flow rate across the whole section is:

$$Q = Nq = -N\frac{\pi a^4}{8\mu}\frac{\Delta p}{l} = -N\frac{\pi a^4}{8\mu\tau}\frac{dp}{dx} \dots\dots eq(12)$$

From assumption, the porosity is:

$$\varphi = N\frac{\pi a^2 l}{AL} \dots\dots eq(13)$$

Recalled that Darcy's law says:

51

$$Q = -k\frac{A}{\mu}\frac{dp}{dx} \dots\dots eq(14)$$

Combining Darcy's law and eq(12), the permeability is therefore:

$$k = \frac{N}{A\tau}\frac{\pi a^4}{8} \dots\dots eq(15)$$

As a result, the modified Kozeny-Carmen equation is:

$$k = \frac{\varphi r^2}{8\tau} \dots\dots eq(16)$$

Besides Kozeny-Carmen equation to predict permeability, permeability in low-porosity

reservoirs can also be estimated from log interpretation using density and neutron

porosity loggings and Coates' method (Crain 2015). Coates simplified the original

Dumanoir-Coates method to calculate permeability from log data and improved the

accuracy especially in low porosity zones by eliminating the number of assumptions.

Coates dictated that:

$$\mathbf{k_c} = \mathbf{5000} * (\boldsymbol{\varphi_e^4}) * \left(\frac{(\boldsymbol{\varphi_t} - \boldsymbol{\varphi_e} * \mathbf{S_{wirr}})}{(\boldsymbol{\varphi_e} * \mathbf{S_{wirr}})}\right)^2 \dots\dots eq(17)$$

Where:

$\mathbf{k_c}$ = calculated permeability, millidarcy

$\boldsymbol{\varphi_e}$ = effective porosity

$\boldsymbol{\varphi_t}$ = total porosity

S_{wirr} = irreducible water saturation

The outcomes of applying modified Kozeny-Carmen equation by assuming tortuosity equals to 1 based on small pore absolute porosity are showed in the left hand side of Table 4. While on the right hand side of Table 4 is the estimated permeability from log interpretation. Noticed that log data for well A is not available. Also, if the core sample is taken from vertical well portion, it is compared with horizontal permeability at the same location and vice versa.

Sample name	k, md (core)	k, md (log)
well B 3-61/72	0.00428	0.0356
well B 4-20/62	0.00280	0.0165
well B 5-10/55	0.00231	0.0170
well C 3-62/66 (Type I)	0.00129	0.00724
well C 3-12/66(Type I)	0.00187	0.0104
well C 1-29/57(Type II)	$4.74*10^{-7}$	$3.86*10^{-6}$
well C 1-18/57(Type II)	$2.54*10^{-7}$	$3.49*10^{-6}$

Table 8. Permeability comparison of Kozeny-Carmen method using core data Coates' method using log data

The permeability estimated using small pores in core samples are much smaller than the outcomes using Coates's method and log data even without considering tortuosity. On the contrary, permeability from core sample are generally larger than that from log interpretation. The most significant reason of such divergence is that the large pores are ignored in this calculation although they do not contribute that much in porosity. For instance, more than 80% of the pores come from small pores in well B, but the permeability from small pores are only 17%. Such fact implies that in tight carbonate reservoirs, small pore or pore throat is not the governing factor for permeability

considerations. The existence of vugs and natural fractures increases the carbonate permeability by one order of magnitude. Also, although the permeability from log interpretation shows optimistic results, the small pores are holding vast amount of hydrocarbon fluids in the reservoir which are almost non-mobile. In this low-kerogen case, no adsorption is taken into consideration during the research. If we are dealing with a high-kerogen case such as Bakken formation, small pores will contribute more to the total porosity but the permeability within small pores will be even smaller due to adsorption.

CONCLUSIONS

Two pore types were identified during the study of Tarim Oilfield. Pore Type I is rich in meso- and macro-pores with an effective pore size of 60-90 nanometers, while Type II contains significant volumes of macropores with larger sizes (>200 nanometers). The wells are rich in Pore Type I with 34-80% of total matrix pore volume due to meso- and macropores. Petrophysical analysis suggests that reliable reservoir storage and flow models to predict the well performances in the field need to be triple porosity, with re-opened fractures imbedded within a matrix that consist of meso- and macropores.

1. Pore size analysis indicates that the samples of wells A and B are dominantly Pore Type I, where as well C has both Pore Type I and II.

2. Pore size distributions are investigated and micro-, meso- and macro- pores contributions are identified. The effective pore size for each sample was estimated using incremental pore-volume weighted averaging. The effective pore size is 58 nm for well A, 82 nm for well B and 63 nm for well C Pore Type I.

3. Pore volume contribution from small pores was identified and compared with the helium porosity. Small pores (<200 nm) of well A has roughly 45%, well B has about 90% and well C has around 34% contribution to the fluid storage. Therefore, a dual porosity model is needed to capture the reservoir system behavior when fractures are not taken into consideration.

4. Well A samples dominantly (more than 70%) consist of dolomite. Both well B and well C are almost 100% calcite. Formation in Well A has experienced high

level of hydrothermal diagenesis. No direct relationship between lithology and pore size distribution is observed.

5. Though significant amount of fluid is stored in the small pores, these pores do not contribute a lot in transportation. Permeability largely depends on larger pores.

REFERENCES

2012. United States. Ministry of the Interior. Department of Energy. U.S. Energy

Information Administration. Sept. 2012.

http://www.eia.gov/totalenergy/data/annual/showtext.cfm?t=ptb0401. (accessed

2 Apr. 2015).

2014. U.S. Crude Oil and Natural Gas Proved Reserves. U.S. Energy Information

Administration, 4 Dec. 2014.

http://www.eia.gov/naturalgas/crudeoilreserves/index.cfm. (accessed 2 Apr.

2015).

Adesida, A. G., Akkutlu, I., Resasco, D. E., & Rai, C. S. 1 January 2011.

Characterization of Barnett Shale Kerogen Pore Size Distribution using DFT

Analysis and Grand Canonical Monte Carlo Simulations. Society of Petroleum

Engineers. doi:10.2118/147397-MS.

Bosboom, Roderic. et al. 2011. Late Eocene Sea Retreat from the Tarim Basin (west

China) and Concomitant Asian Paleoenvironmental Change. *Palaeogeography,

Palaeoclimatology, Palaeoecology.* **299**(3-4): 385-398. doi:10.1016/S0031-

0182(10)00740-6.

Chai, Guilin, et al. 1 Jan 1991. Petroleum Geology and Oil Potential of Tarim Basin,

West China. World Petroleum Congress. WPC-24102

Chayes, F. 1954.The Theory of Thin-Section Analysis. *The Journal of Geology.* **62**(1):

92-101. DOI: 10.1086/626135

Crain, E.R. 2015. The Common Permeability Methods. *CRAIN'S PETROPHYSICAL POCKET PAL*. Jan 2015, https://www.spec2000.net/01-permeability.htm. (accessed 16 May 2015).

Dutrow, Barbara L. 2012.X-ray Powder Diffraction (XRD). *Science Education Resource Center (SERC) at Carleton College*. 14 Dec. 2012, http://serc.carleton.edu/research_education/geochemsheets/techniques/XRD.html . (accessed 12 Feb. 2014).

Halbertsma, H.L. 2012. Devonian Wabamun Group of the Western Canada Sedimentary Basin. *Alberta Geological Survey*. Alberta Energy Regulator. (accessed 11 Sep. 2012). http://www.ags.gov.ab.ca/publications/wcsb_atlas/a_ch13/ch_13.html. 9 Feb. 2015.

He, Feng, et al. 2015. Sedimentary Facies and controlling Factors of Yingshan Formation in Gucheng area, Middle-Lower Ordovician, Tarim Basin. *EJGE* 20(3): 919-925.

Hirsch, Dave. 2012. How to make a thin section. *West Virginia University Geology Department*. West Virginia University. Oct. 2012. http://geology.wwu.edu/dept/faculty/hirschd/other/thinsections/. (accessed 12 Feb. 2014).

Micromeritics. 2008. Gas Adsorption Theory. http://www.micromeritics.com/Repository/Files/Gas_Adsorption_Theory_poster. pdf. (accessed 12 Feb. 2014).

Micromeritics. 2008. Smart VacPrep Gas Adsorption Sample Preparation Device.
Micromeritics Showcase. Micromeritics. http://www.micromeritics.com/Product-
Showcase/Sample-Preparation-Systems/Smart-VacPrep.aspx. (accessed 12 Feb.
2014).

Micromeritics. 3Flex Surface Characterization Analyzer. Micromeritics Showcase.
http://www.micromeritics.com/Product-Showcase/3Flex-Surface-
Characterization-Analyzer.aspx. (accessed 12 Feb. 2014).

PennState Marcellus Center. 2012. How Much Natural Gas Can The Marcellus Shale
Produce?. Pennsylvania State University College of Earth and Mineral Sciences,
May 2012. http://www.marcellus.psu.edu/news/PDFs/gasreserves_day.pdf.
(accessed 18 June 2015).

Purser B. H., Brown A., Aissaoui. 1994. Nature, origins and evolution of porosity in
dolomites. IAS Spec Publ, 21: 283-308.

Rust, William, and Amy Cushing. 2001. The Buried Silk Road Cities of Khotan. *Athena
Review*. **3** (1):23.

Su, Nan. 2015. The Potential of Natural Gas is Much Larger than Oil in China. *China
Energy News*. 11 May 2015: A2.

Swapp, Susan. 2012. Scanning Electron Microscopy (SEM). *Science Education
Resource Center (SERC) at Carleton College*. Carleton College. 14 Dec. 2012.
http://serc.carleton.edu/research_education/geochemsheets/techniques/SEM.html
. (accessed 12 Feb. 2014).

The New Mexico Institute of Mining and Technology. Porosity – Permeability

Relationships. 2010. *The New Mexico Institute of Mining and Technology*

Department of Petroleum & Natural Gas Engineering.

http://infohost.nmt.edu/~petro/faculty/Engler524/PET524-perm-2-ppt.pdf.

(accessed 15 Sep. 2015).

Yun, Lu, Zhigao Xiao, and Mingjun Xu. 2015. A Discussion on Natural Gas Exploration

in Tarim   Basin. *Gasshow*. Sinopec NW E&D Corporation, 21 Feb. 2005.

http://news.gasshow.com/News/SimpleNews.aspx?newsid=179097. (accessed 16

June 2015).

Zhao, Wenzhi, et al. 2014. The porosity origin of dolostone reservoirs in the Tarim,

Sichuan and Ordos basins and its implication to reservoir prediction. *Science*

China **57**(10):2498-2511. doi:10.1007/s11430-014-4920-6.